Mechanical Characterization of Additive-Manufactured Ti-6Al-4V Processed via Bound Metal Deposition

Devine E, Lester M, McElroy T, Valenzuela T, LePage W

PUBLISHED AS

Devine E, Lester M, McElroy T, Valenzuela T, LePage W. "Mechanical Characterization of Additive-Manufactured Ti-6Al-4V Processed via Bound Metal Deposition." Experimental Mechanics 65, 573-596 (2025).

https://doi.org/10.1007/s11340-025-01178-x

Mechanical characterization of additive-manufactured Ti-6Al-4V processed via bound metal deposition

E.T. Devine[1], M.R. Lester[1], T. McElroy[1], T. Valenzuela[1], and W.S. LePage[1†]

[1]Department of Mechanical Engineering, University of Tulsa, Tulsa, OK, 74104, USA
[†]Correspondence: lepage@utulsa.edu

Abstract

Background: Additive manufacturing (AM) is rapidly growing, with new AM methods continually in development. Alloys processed with novel methods require systematic characterization to understand and validate the materials, especially for demanding fields. **Objective**: This study characterized the mechanical properties and failure mechanisms of a Ti-6Al-4V alloy manufactured with bound metal deposition (BMD), a form of metal extrusion (MEX) AM. **Methods**: Specimens made of Ti64 were printed via Desktop Metal's Studio System 2 through a printing, debinding, and sintering process. The microstructure was analyzed with optical metallography and a newly developed open-source porosity analysis tool. Scanning electron microscopy (SEM), optical microscopy, and compositional analysis of green, brown, and sintered parts were conducted to study the material and its failure modes. Sintered specimens were tensile and hardness tested. **Results**: As-sintered specimens exhibited ductility more than 10 times lower than wrought Ti64, partially due to contamination/impurity that formed brittle α-case titanium. Sources of contamination may have included the sacrificial Al_2O_3 interlayer, the wax/polymer binder, and/or impurity introduction from the furnace. Fractography imaging found quasi-cleavage fracture initiating at areas of high surface roughness along the ceramic interlayer surface of the parts and transitioning into dimple rupture and intergranular decohesion. **Conclusions**: Elevated contamination levels, high surface roughness, and internal porosity led to low elongation and ultimate strength in the Ti64 BMD alloy. With the processing route presented here, BMD for Ti64 may not be suitable for applications that demand high ductility and strength with minimal impurities, although with process refinement, the method may be promising for certain applications.

Acknowledgments

The authors gratefully acknowledge support from the University of Tulsa and the Engineer Research and Development Center (ERDC) under Contract No. W912HZ-23-C-0009. The authors also acknowledge the contributions of Dr. Philip Noell during the editing and revision of this manuscript.

Keywords: Additive manufacturing, material extrusion, titanium, contamination, fracture, elongation

1. Introduction

Conventional/wrought Ti-6Al-4V (Ti64) is known for its low density, high specific strength, and high corrosion resistance, making it essential to many sectors such as aerospace, automotive, biomedical, energy, and others.[1–4] Specific applications include jet engine components such as fans, compressors, turbine blades, impellers, airframes, rocket engine components, heart valves, bone and dental implants, automotive springs, and bicycle frames.[1,2,4,5] Ti64 is not as easily produced and machined with conventional methods as other common alloys, making it a good candidate for additive manufacturing (AM) techniques.[3] One of the advantages of using AM for Ti64 is the superior strength of the material when compared to conventional methods, although

ductility is often lower.[3]

AM allows parts to be built one layer at a time to form part geometries that are not possible with traditional processing techniques.[6] AM parts are known for their low weight and production time across industries with demanding requirements.[3,7–10] Nonetheless, new challenges arise related to the mechanical properties of the materials, including lower fatigue life, high surface roughness, metallurgical defects, low dimensional tolerance, low plasticity, and low ductility.[3,6,7,11,12] AM parts must often be post-processed via heat treatment or surface treatment after production due to these shortcomings.[3] Because these issues can significantly influence the life of the part in service, more work is needed to understand the mechanisms at play in materials processed with different AM methods.

ISO/ASTM 52900:2021 outlines seven types of AM techniques as follows: binder jetting (BJT), direct energy deposition (DED), material extrusion (MEX), material jetting (MJT), powder bed fusion (PBF), sheet lamination (SHL), and vat photopolymerization (VPP).[13] Of these, DED, PBF, and SHL are direct metal AM methods, in which the part is directly processed into the final part without intermediate steps such as sintering.[6] In indirect metal AM, the four other AM techniques can be used to form the "green" part or build the tools needed to finish the part.[6,14] For the production of Ti64 alloys, only the direct methods DED, PBF and SHL had been utilized until recently.[3,9] These methods are extremely useful to many sectors, but they also have disadvantages such as high system cost and exposure to dangerous metal powders or chemicals.[7,15,16]

Many industries would benefit from safer, lower cost, and faster AM methods that do not sacrifice material properties. An MEX, indirect method termed bound metal deposition (BMD) has been developed by Desktop Metal using their Studio System 2 for the production of metal alloys. It is a lower startup cost and lower production volume option than many other AM methods[15,17–21], while being safer and more accessible because it does not involve the use of loose metal powder or high energy lasers.[15,16,22,23] Desktop Metal launched a Ti64 alloy in 2021 compatible with their Studio System 2, which has not been extensively characterized in the literature. In addition to Ti64, they also supply 17-4 PH stainless steel, 316L stainless steel, 4140 low-alloy steel, A2 tool steel, H13 tool steel, copper, and Inconel 625 alloys for the Studio System.[24] This AM method is considered to be a form of fused filament fabrication (FFF). Another similar method in this category includes metal extrusion atomic diffusion AM (ADAM) used by the Markforged Metal X system[18,25] which uses a spool of filament rather than cylindrical rods.[7] Additionally, BASF produces its Ultrafuse filament in 316L and 17-4 PH stainless steels[26], which can be used with an FFF printer and a lab tube furnace.

BMD utilizes build media in the form of rods consisting of pre-alloyed metal powder bound in a polymer and wax matrix. These rods are extruded via a plunger through a heated nozzle, similar to some thermoplastic AM systems. The part is printed layer-by-layer until it is complete. At this point in the process, it is designated as a "green" part. Next, the material must undergo a debinding process to remove the polymer and wax from the bulk part. This can be performed using a chemical solvent followed by a thermal debinding step, or by using the thermal debinding step alone. After the debinding process, the "brown" part is heated in a furnace to sinter it and form a near fully dense metal part (often above 97% relative density) similar to metal injection

molding (MIM). Though commercial MEX Ti64 processes are relatively scarce in the literature, some have characterized MEX Ti64 properties, which will be discussed later.[27–29] There are several studies reporting on the properties of 316L and 17-4 PH stainless steel produced with MEX,[16,18,19,21,30–36] and on copper produced with BMD.[20,37]

This work is the first to characterize the mechanical properties of "as-printed" Ti64 samples produced via BMD without machining after sintering. Optical and SEM images were taken to view the microstructure and measure porosity. Energy dispersive spectroscopy (EDS) was performed to evaluate the ternary alloy composition, and inert gas fusion was used to measure oxygen, nitrogen, and hydrogen contamination, while the combustion method was used to measure carbon content in the samples. Microhardness testing and tensile testing were conducted on "as-sintered" samples, which were not post-machined, to find ultimate tensile strength (UTS) and elongation values. Finally, fracture surfaces were studied to determine fracture mechanisms.

2. Methods

2.1 Materials and processing

AM samples of this study were produced via the Desktop Metal Studio System 2 using BMD. All BMD samples in this work followed the manufacturer-supplied procedures. In the BMD process, parts were designed in SolidWorks, converted to an STL file, and imported into Desktop Metal's FabricateStudio software (v 2.19.17). The total build volume is $305 \times 200 \times 200$ mm, but due to shrinkage during sintering, the effective final part volume is actually $240 \times 160 \times 160$ mm.[38] The vendor-recommended size range for any single part produced with the printer is between $6 \times 6 \times 6$ mm and $110 \times 110 \times 110$ mm, to ensure binder can penetrate fully into the part, though this is a conservative value. The estimated cost of material for each part given by the Fabricate software was $24.96. In the printing step, rods containing the pre-alloyed metal powder and a polymer-wax matrix are heated by the extruder nozzle to print the part layer by layer.[39] Four to five samples were printed at a time in one row along the back edge of the build plate to minimize the sample distance from the rigid lead screw at that location. This was done to reduce deflection of the build plate and possible error in the system as the print nozzle moved away from the rigid mounting point. The print time was 17 h 49 m for four samples . The layer height was set to 0.20 mm, and both the wall and the top/bottom layer thicknesses were set to 4.5 mm with a total of 46 layers per part.

The gauge section itself consists of 12 print layers running along the X direction without gaps for full density, as seen in **Fig. 1(a)** and **Fig. 1(b)**. Other studies have found that tensile specimens perform better when the rasters run parallel to the loading direction.[18,21,33,36] Portions of the grip sections contain infill with an alternating 45° pattern and a default green density setting of 17.14%. The print speeds were left at the default values. The software allows the user to apply a scale multiplier to the parts to account for shrinkage during sintering. The default value is 1.16, which results in a green part that is 16% larger than the designed final dimensions. If the scale factor is accurate, the part will shrink about 16% during sintering to closely match the desired dimensions. In this work, the final dimensions were not as important as measuring how much the parts actually shrank, so a scale factor of 1.00 was used. All samples were printed with a "raft"

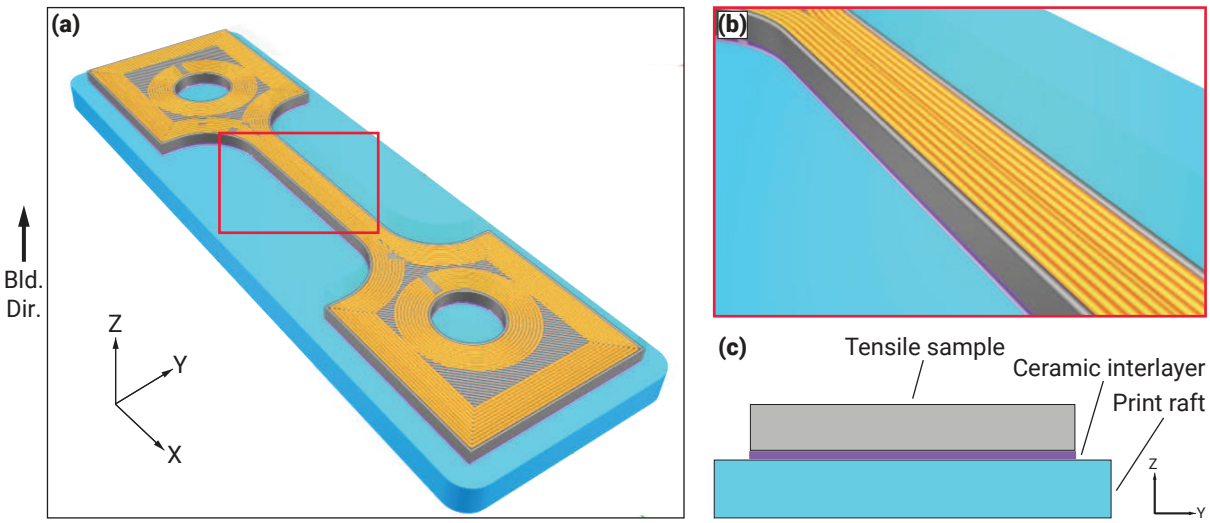

Fig. 1: *(a) The sample rendered in FabricateStudio software showing the (b) print layers aligned in the X direction along the gauge section. (c) The tensile sample is lightly adhered to a print raft (also made from Ti64) via a ceramic interlayer.*

which also consists of Ti64 and lightly adheres to the part via a ceramic interlayer as shown in **Fig. 1(c)**. This raft increases adhesion to the build surface, facilitates uniform shrinkage during sintering, reduces warping, and acts as a stable base for the part.[40] The non-sintering ceramic interlayer is used to allow the part to release easily from the raft and to allow support structure to be removed without expensive post-machining after sintering. The interlayer is printed in a single layer under the part with a thickness range of 0.15–0.3 mm. The estimated green part mass given by the software was 65.26 g with the raft, the estimated brown part mass was 61.64 g, and the estimated sintered part mass without the raft was 21.05 g. The actual average green part mass was 70.25 g, the average brown part mass was 66.25 g, and the average sintered mass without the raft was 23.40 g.

After printing, all 12 green parts in this batch were chemically debound at once using a solvent to dissolve a portion of the binder.[39] The main parameter affecting debind time is the maximum cross-sectional area of the largest part in the debinder as well as the density of the parts. A typical debind cycle took around 41 h per batch. The debinding step forms a porous structure in the part, which allows the polymer binder material to be removed during a thermal debind phase in the furnace.[39] The polymer begins evaporating between 200°C and 600°C, and the furnace holds within this temperature range until all the binder is removed.[39]

The full part, including the raft, is placed in the furnace on zirconia setter plates fitted onto graphite retort shelves. The setters prevent contact of the metal parts with the graphite shelves.[41] After the second thermal debinding phase in the furnace, the furnace reaches its maximum temperature and the part is sintered into a near fully dense part. The thermal debinding and sintering process is completed under vacuum with ultra high purity argon (UHPA), which is 99.999% pure, as a shielding gas, and two zirconium pucks that act as oxygen getters. The thermal debinding, sintering process, and furnace cooling normally take around 1–3 days, although it could take up to 4–5 days when approaching the mass limit for the furnace.

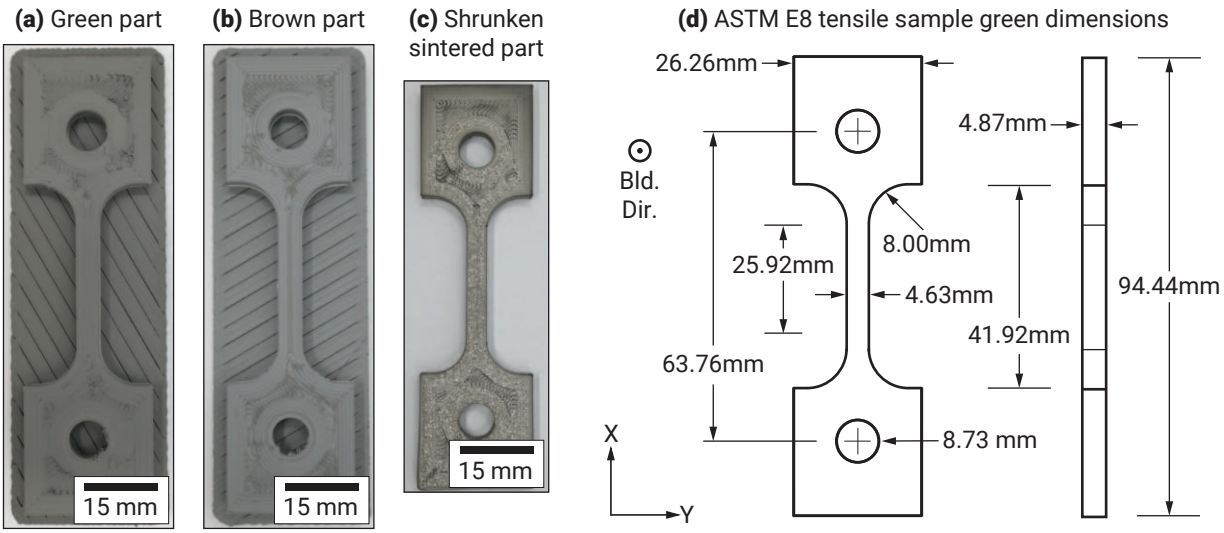

Fig. 2: *(a)–(c) Images of the green, brown and sintered parts and (d), the tensile specimen green part dimensions. The sheet samples were cut using the average sintered part dimensions of the BMD samples rather than the green part dimensions so that they matched the reduced size of the sintered parts as closely as possible.*

Fig. 2(a)–(c) show a sample in each processing condition. Note the color change between each condition and the general glittery appearance of the sintered part. There is some discoloration on the outer edges of the part as well, which can indicate oxygen contamination. The sintered samples were removed from the rafts, tested in the as-sintered condition, and no post-processing or machining was performed.

The furnace does not display the exact temperature profile during sintering. However, a recent study on BMD processing of Desktop Metal's Ti64 suggests a peak sintering temperature of approximately 1130°C.[27] In the present study, two resistance temperature detectors (RTDs) were placed onto the furnace outer surface during a sintering run and the temperature profile was recorded and plotted in **Fig. S1**. The gas flow rate of UHPA was also recorded in the same figure. The total sintering cycle took about 3000 min or 50 h, over double that of the cycle published in Tuncer et al.[27] This increase in time is likely due to the fact that more mass was present in the furnace cycle of the present study than in the cycle in Tuncer et al.

BMD tensile samples were produced in accordance with ASTM E8 as seen in **Fig. 2(d)** and will be referred to simply as BMD samples. As-received grade 5 titanium (Ti64) sheet in the annealed condition was purchased and cut into tensile samples with the rolling direction oriented parallel to the tensile axis to serve as a control. These will be referred to as "as-received sheet samples." The samples were cut using an OMAX ProtoMAX abrasive water jet cutter based on the average dimensions of the BMD samples rather than the green dimensions provided in **Fig. 2(d)**. In addition to the control samples, additional sheet samples were placed in the furnace along with the BMD samples to observe the effects of the furnace cycle on the properties and microstructure of the sheet material. These are called furnace treated (FT) sheet samples from now on. There were a total of 12 BMD and four FT sheet samples in this sintering cycle. A summary of the sample types and processing conditions is in **Table 1**.

Table 1: *Sample names and processing conditions for this work.*

Sample name	Condition
As-received sheet	Grade 5 titanium sheet as-received, annealed
FT sheet	Grade 5 titanium sheet furnace treated alongside BMD samples
BMD sample	As-sintered

Part dimensions were measured using digital calipers (Mitutoyo Absolute Digimatic Solar Caliper) with a precision of 0.01 mm in the green, brown, and sintered states, and the corresponding part shrinkage in each dimension was characterized. Additionally, the mass loss during chemical debinding and sintering was measured with a precision of 0.001 g.

2.2 Composition analysis

EDS was performed on the parts using TEAM Enhanced software (version 3.4.1) with an accelerating voltage of 10kV to obtain maps of the elemental content of the alloy. Due to low resolution, EDS is sufficient only in determining the content of high percentage alloy constituents (e.g. titanium, aluminum, and vanadium) and not for determining the lower percentages of contaminants such as oxygen, nitrogen, carbon, and hydrogen which can embrittle the material. Inert gas fusion was used to characterize hydrogen, nitrogen, and oxygen in the specimens using a Bruker Galileo G8 for oxygen and nitrogen and a Leco RH-404 for hydrogen. The combustion method was performed on the samples to measure carbon content in the specimens using a Leco CS-844. EDS point analysis was performed on the unsintered ceramic interface rod build media to determine its composition.

2.3 Optical metallography, microscopy and porosity analysis

Cross sections were taken from the gauge sections of fractured tensile specimens for optical metallography and porosity analysis. The samples were cut using an Allied High Tech PowerCut 10x abrasive cut-off saw and mounted in a two-part epoxy. Two polishing recipes were used for sample preparation. The sample shown in **Fig. S2(a)** was polished using method A. In method A, the sample was wet sanded sequentially with 120/320/600/800/1200 grit sandpaper for 1–3 min at each step. Polishing was completed with 1 μm alumina and 0.06 μm colloidal silica (MasterMet® Colloidal Silica) mixed with 30% hydrogen peroxide in a volume ratio of 4:1 for 3–5 min at each step or until all scratches from the previous step were removed. In the more optimized method B, the remaining samples were wet sanded with 320/600 grit sandpaper for 1–3 min at each grit. Polishing was completed with a 9 μm diamond suspension followed by a 0.25 μm diamond suspension before finishing the polish with the 0.25 μm colloidal silica (MasterMet® Colloidal Silica) and hydrogen peroxide mixture specified in method A. Method B reduced rounding at the edges and pores of the parts. Samples were etched by immersion for 5–10 seconds in Kroll's reagent. The samples were polished for another 5–10 seconds using the colloidal silica mixture before ultrasonic cleaning in 1:1 deionized (DI) water and isopropyl alcohol (IPA) solution. Images were taken with a Nikon Epiphot 200 inverted metallographic microscope and images were stitched together with a custom MATLAB script and Microsoft ICE.

A MATLAB script was used to measure porosity on polished samples. The contrast was adjusted by changing the pixel intensities to accurately identify pixels in pore regions of the samples. Images taken for porosity analysis were stitched together from images with a horizontal field width of 768 μm (20x magnification). **Fig. 3** shows how the script takes a raw image (**Fig. 3(a)**) and maps a user-defined set of pixel intensity values to another higher contrast set of values in order to more accurately measure the porosity in the image. **Fig. 3(b)** shows the raw image with the pixels associated with pore regions colored in blue. Finally, the image is binarized as shown in **Fig. 3(c)**, and the porosity is calculated as the ratio of pore pixels to the number of total pixels in the image. Three total cross sections were imaged and analyzed from three different BMD samples and the overall porosity was calculated. The interlayer porosity, or porosity between the print layers, was calculated by taking 24 cropped images between the print layers for each of the three cross sections. These regions were randomly selected by arbitrarily defining a cropping area between the print layers (which are easy to visually distinguish) within the overall image. The three sets of 24 images were analyzed and binarized via the same method as the overall porosity images, as seen in **Fig. 3(d)–(f)**. The 24 porosity values for each of the three images were then averaged and the porosity values were obtained.

Raw build media, as-sintered, brown, and green part samples were imaged using a Helios NanoLab 600 scanning electron microscope (SEM) using Everhart–Thornley detection (ETD) and backscattered electrons to inspect the raw surfaces of the green, brown, and polished cross sections of the samples.

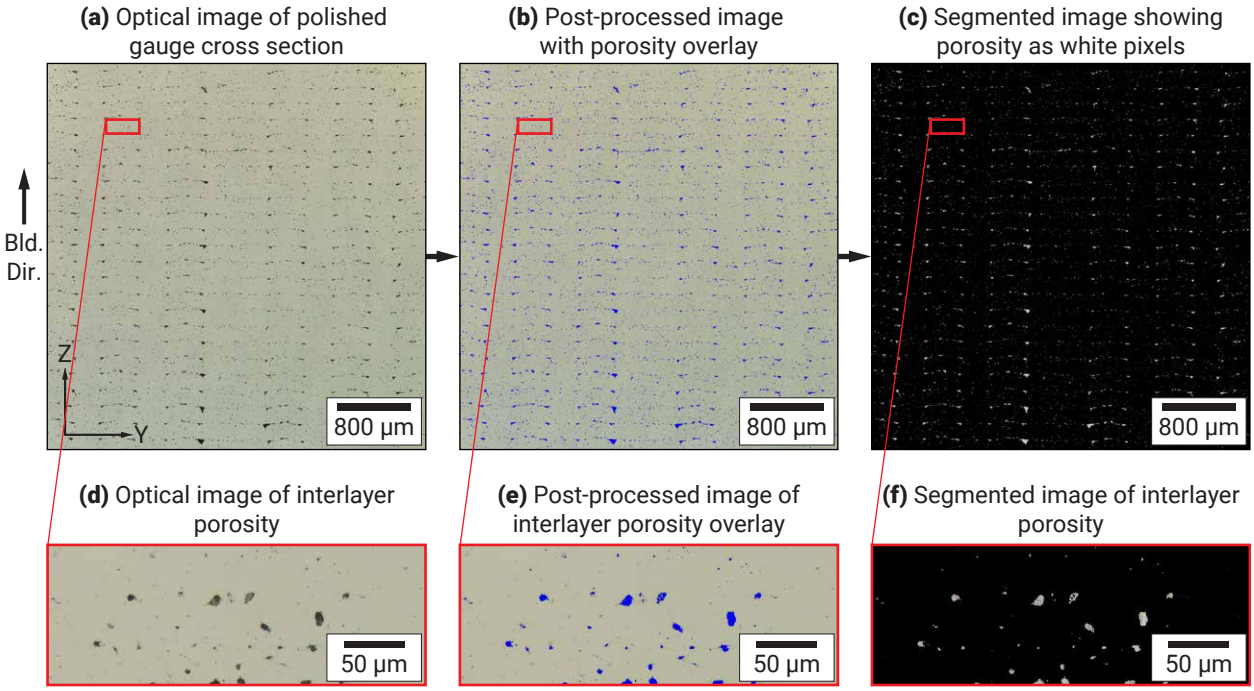

Fig. 3: *(a) Optical image of polished BMD cross section taken from specimen gauge, (b) post-processed image with a threshold of dark pixels defined as porosity and colored in blue, and (c), the segmented image showing porosity as white pixels with (d), (e), and (f) showing magnified views of interlayer porosity from the same images.*

2.4 Mechanical testing

Hardness testing

Two series of microhardness tests were performed. In the first, Knoop microhardness measurements were performed with a Leitz Miniload hardness tester with an application force of 200 g. Indentations were applied to a polished cross-section of a BMD sample and an FT sheet sample with an application time of 14 seconds, and a dwell time of approximately 10 seconds. Indentations were applied in groups of 4–8 to the bottom, left, middle, right, and top of two BMD samples, two FT sheet samples, and one as-received sheet sample as shown in **Fig. S2**.

In the second series of testing, Knoop and Vickers measurements were performed with the Leitz Miniload through the depth and width of the BMD and FT sheet samples. The application force for the Knoop tests was 200 g while the force for the Vickers tests was 500 g. The application and dwell times remained the same. A 500 g force was used for Vickers testing to provide a more accurate bulk hardness measurement than Knoop can achieve at 200 g. For the BMD sample, three Knoop and Vickers measurements were performed and averaged per depth increment. The Knoop depth increment was 4 thousandths of an inch or 0.1016 mm and the Vickers depth increment was 6 thousandths of an inch or 0.1524 mm since Vickers indentations cannot be as closely spaced per ASTM E384. The indentations begin at the ceramic interface surface and progress in the build direction toward the top of the sample. For the FT sheet sample, three Knoop measurements were performed and averaged per depth increment in the horizontal and vertical directions. One Vickers measurement was performed per depth increment in the horizontal and vertical directions. For all testing, the Nikon Epiphot 200 was used to image and measure indentation dimensions to calculate hardness.

Tensile testing and fractography

The specimens were tensile tested on an MTI load frame until failure using displacement control and a displacement rate of 0.012 mm/min which corresponds to a strain rate of $5 \times 10^{-6} s^{-1}$ for the BMD and FT sheet sample. This value is within the quasi-static regime for Ti64 where the main deformation mechanism is planar slip within α grains and not deformation twinning, though some deformation twinning still occurs.[42,43] Studies have reported strain rates in this regime ranging from $1 \times 10^{-3} s^{-1}$ to $1 \times 10^{0} s^{-1}$ with some values as low as $1 \times 10^{-5} s^{-1}$.[42–44] The as-received sheet sample displacement rate was increased to 1.2 mm/min to speed up testing, but this value is still quasi-static. Two 12.3-megapixel camera sensors (FLIR GS3-U3-123S6M-C) were used with Edmund Optics HP Series 50 mm fixed focal length lenses (model #86-574) for stereo optical digital image correlation (DIC) with cross polarization (which decreases over-saturated pixels and increases contrast)[45] to measure the strain field during loading. 20 mm extension tubes (Computar VM100 kit) were used to provide the best field of view (FOV) and sample magnification. An AmScope HL250-A 150W Fiber Optical Microscope Illuminator was used to light the specimens during testing, and Midopt® PRO32-37.5 and PRO32-22.5 linear filters were used on the camera lenses and lights for cross polarization. Samples were painted with a white base coat and black speckles to take advantage of the higher hiding power of the black paint and to reduce error in the DIC results.[46] An image of the DIC setup can be found in **Fig. S3** and detailed DIC software and hardware reports can be found in **Table S7** and **Table S8** as recommended by the International Digital Image Correlation Society

(IDICs).[47] Fracture surfaces of the specimens were imaged using the SEM with ETD. SEM images were stitched together using a custom MATLAB script and Microsoft ICE to image the entire fracture surface with high resolution.

3. Results and discussion

3.1 Part shrinkage and mass loss

The mass of the BMD tensile specimens in each condition is shown in **Fig. 4(a)**. They exhibited an average mass loss of 4.00 g (6.0%) between printing and chemical debinding, and a mass loss of 2.78 g (4.4%) between chemical debinding and sintering for a total mass loss of 6.78 g per sample on average. This is a 9.7% reduction in mass. They had an average shrinkage of 14.1% in all three dimensions. The shrinkage in each dimension is shown in **Fig. 4(b)**. Full tables with dimension and mass data for the green, brown, and sintered parts are in **Tables S1–S3**. The Z direction experienced the most change at 18.0%, due to gravity acting in the negative Z direction. This anisotropic shrinkage result has been observed in other works.[21,32,35,36,48] This force caused a larger reduction in the thickness of the part, while also counteracting the shrinkage in the X direction (at 12.0%) and Y direction (at 12.4%), similar to the inverse relationship of Poisson's ratio. Another contributing factor to the increased shrinkage in the Z direction is likely to be the high concentration of porosity along the Y axis, resulting from gaps between print layers. Desktop Metal's default 1.16 scale factor applied to their parts at the printing step is a close approximation of the actual average shrinkage of 14.1%, though it is a slight over-correction. These values are within the typical range for shrinkage found for MEX and MIM Ti64 which is between 12% and 15%[27,28,49], and 12% and 20%, respectively.[50] Shrinkage is essentially the same for MEX 316L and 17-4 PH which is 12% to 23%.[21,32,35,36,48,50] Part geometry and print parameters are both important factors that could change the overall shrinkage, and it might take trial and error to get the correct dimensional tolerance for certain geometries. Overall, dimensional tolerance may be inconsistent, especially when using different geometries, and precise parts may need to be post-

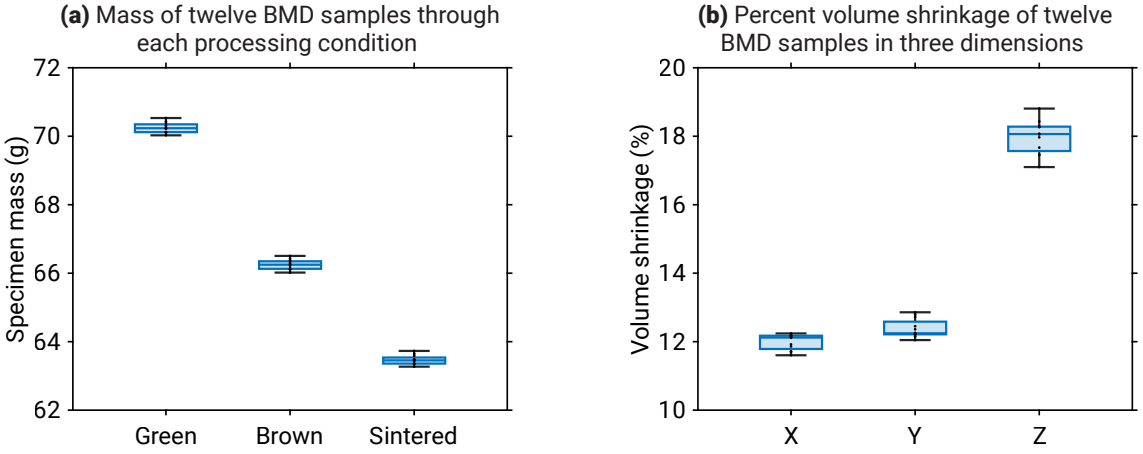

Fig. 4: *(a) Mass of specimens in the green, brown and sintered state, showing a linear downward trend through each condition, and (b) the percent volume change in the X, Y, and Z directions. The Z direction has the largest shrinkage, due to the effects of gravity acting in the negative Z direction during sintering.*

machined.

3.2 Composition

Ti64 is very susceptible to interstitial oxygen contamination at elevated temperatures around 400°C–600°C.[1,51] Ti64 is an $\alpha - \beta$ titanium alloy with 6 wt% aluminum acting as an α phase stabilizer and 4 wt% vanadium acting as a β phase stabilizer.[1,4] Oxygen stabilizes the higher strength α phase, increasing UTS but lowering ductility.[1,52,53] Other important α stabilizing contaminants include nitrogen and carbon. The effects of each on the α phase can be expressed in the oxygen equivalent formula: $O_{\text{eq}} = O + 2N + 0.75C$, showing that nitrogen has the largest effect and carbon has the smallest effect. Hydrogen stabilizes the β phase and is known to cause embrittlement, which is why the grade 5 titanium specification limits hydrogen to 0.015 wt%.[1,54] Impurities are introduced via oxides on pre-alloyed powders, through the debinding or sintering atmosphere, or through physical contact with materials in the

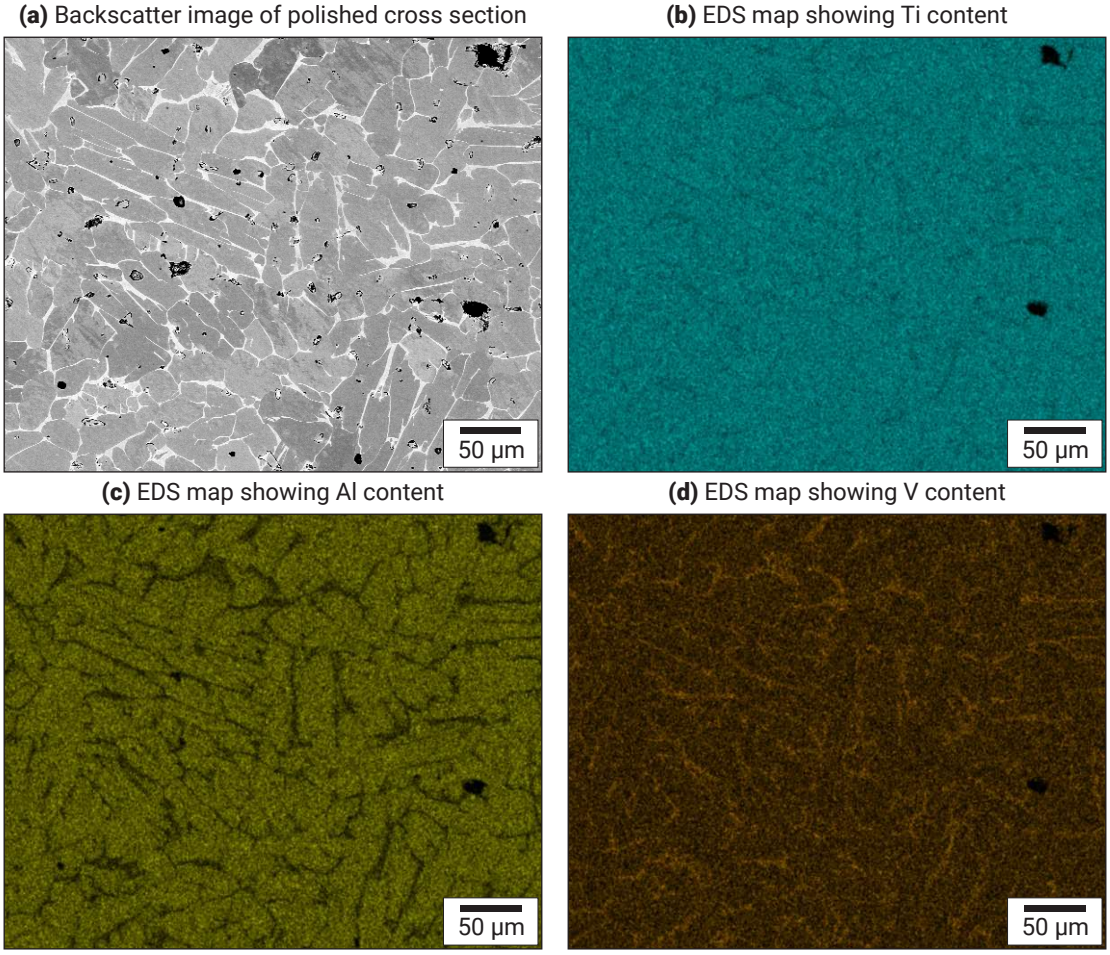

Fig. 5: *(a) Backscatter imaging of a BMD sample gauge cross section showing the $\alpha - \beta$ microstructure. (b) EDS map showing titanium (89.52 wt%), (c) aluminum (6.74 wt%), and (d), vanadium (3.75 wt%) content with the same FOV as the backscatter image.*

furnace.[51,55] German et al. note that a vacuum pressure of $1 \times 10^{-4} Pa$ or lower is required to keep impurity levels in check[56] and it is unclear whether the Desktop Metal furnace vacuum pump maintains these low pressures. It is also possible that small leaks in a furnace system could introduce significant contamination.

EDS provided information about the quantities of the larger alloy constituents of this work. **Fig. 5** shows the EDS results along with a high resolution backscatter image of the BMD microstructure. **Fig. 5(b)** shows the relatively uniform distribution of titanium throughout the bulk microstructure, though the α laths show a slightly larger concentration of it. **Fig. 5(c)** shows aluminum content with a strong preference for the α phase as expected, while **Fig. 5(d)** shows the vanadium content with a higher concentration in the β phase. This analysis yielded an overall composition of 89.52 wt% titanium, 6.74 wt% aluminum, and 3.75 wt% vanadium which is within the limits of the grade 5 specification.[54] A previous study noted that the ceramic interface material for the Studio System 2 is aluminum oxide (Al_2O_3).[27] The point analysis on the ceramic interface build media yielded a composition of primarily carbon, oxygen, and aluminum, confirming that the ceramic interface material is aluminum oxide mixed with a binder. It is probable that the Al_2O_3 reacted with the Ti64, causing aluminum and oxygen to diffuse into the sample at this interface, leading to the formation of α-case titanium, as discussed in later sections. The carbon content originates from the polymer binder.

The contaminants oxygen, nitrogen, carbon, and hydrogen were measured and the values are reported in **Table 2** along with the oxygen equivalent value which is calculated via the equation $O_{eq} = O + 2N + 0.75C$.[51] Notably, the as-received sheet is in compliance for all the elements as indicated in green text in Table 2. The FT sheet was not in compliance for oxygen, while the two BMD samples analyzed were not in compliance to a higher degree in oxygen. The carbon content was significantly higher in the BMD samples, though still within the specification. Values outside of compliance are indicated in red. This led to a significantly higher O_{eq} value for the BMD samples. The contamination found in the FT sheets must have been introduced via system leaks (perhaps around the large furnace O-ring) or insufficient vacuum pressures. It is unlikely to originate from the UHPA shielding gas. The higher contamination levels in the BMD

Table 2: *Oxygen, nitrogen, hydrogen, and carbon contamination levels in four samples. The first sample is an as-received sheet acting as the control, the second is a FT sheet sample, and the last two are BMD samples.*

Sample condition	Oxygen	Nitrogen	Hydrogen	Carbon	Oxygen equivalent
ASTM B265 standard	≤0.20	≤0.05	≤0.015	≤0.08	- -
As-received sheet	0.20	0.01	0.0036	0.02	0.235
FT sheet	0.24	0.01	0.0020	0.04	0.290
BMD-1	0.39	0.03	0.0025	0.08	0.510
BMD-2	0.30	0.03	0.0026	0.07	0.413

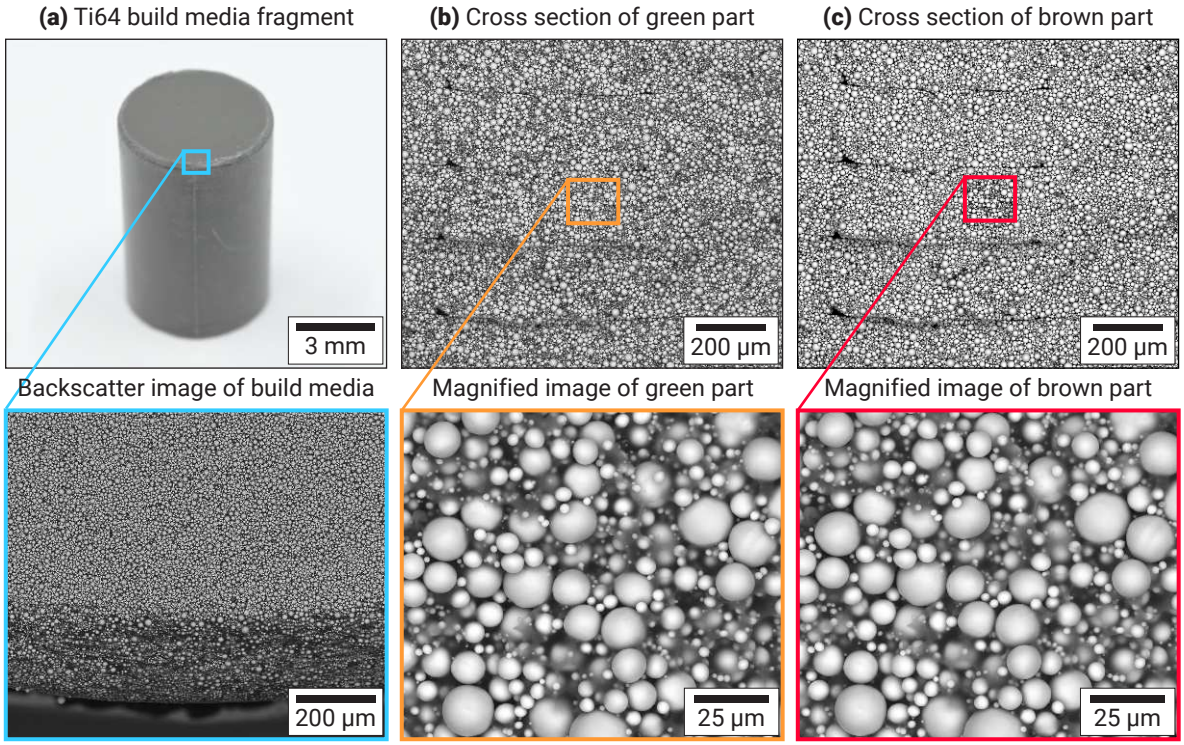

Fig. 6: *(a) Optical and SEM imaging of rod-like build media consisting of Ti64 pre-alloyed powder and a polymer binder. (b) SEM imaging of a green part and (c) SEM imaging of a brown part after chemical debinding.*

samples must be originating from a source other than leakage, unless significant contamination was already present on the powder particles, which is unlikely. This extra contamination most likely comes from the Al_2O_3 ceramic interface material in the form of oxygen and aluminum. Further evidence of oxygen contamination is provided by the dark coloring of the sample along its outer edges and especially on the ceramic interface surface. A work by Carroll et al. has drawn a connection between dark discoloration in AM titanium, and oxygen contamination.[57] The presence of elevated oxygen in both the BMD and FT sheet samples could cause the formation of α-case, which was further investigated in later sections.

3.3 Structure

The build media microstructure in **Fig. 6(a)** shows the Ti64 powder suspended in the polymer and wax matrix. **Fig. 6(b)** shows the green part, while **Fig. 6(c)** shows the brown part microstructure. It is interesting to note that the two microstructures appear almost identical, though there was a chemical debinding process that took place between the acquisition of each image. From the images, **Fig. 6(c)** appears to have more void space than **Fig. 6(b)** due to the removal of wax. Polymer binder is still visible in both images and appears as the semi-transparent non-spheroidal dark regions. The thermal debinding process is likely designed to remove the rest of the polymer binder. The large void space between each print raster seen in these images perpetuates after the sintering process, resulting in lack-of-fusion porosity in the final parts as discussed in Section **3.4**.

The microstructure of AM and MIM Ti64 is critical to understanding its mechanical behavior. It is desirable to have a fine, equiaxed grain structure for optimal mechanical properties. AM processing methods, heat treatment, system power and alloy purity can significantly affect the volume percentages and grain size of these two phases, and shift the martensite start temperature.[3] For electron beam melting (EBM) and DED, several studies have shown that the β grains in a build layer form with a similar orientation as the previous build layer, but perpendicular to the melt pool.[58–60] This typically produces a columnar β structure with grain sizes ranging from 0.2 mm to 4 mm for DED.[3,52,61] Though useful for certain applications, this textural bias can cause high anisotropy, leading to cracks forming more easily along the prior β grain boundaries.[19,62] Several works have produced smaller equiaxed grains via different methods including nanoparticle grain inoculation in LPBF AM aluminum alloys that induced small grain nucleation[63], process refinement in wire-arc AM that reduced the thermal gradient in the melt pool[62], and ultrasonic exposure of the melt pool to cause cavitation and grain nucleation.[64,65] These studies aimed to allow supercooled solute to exist ahead of the solidification front to promote homogeneous nucleation and formation of small, equiaxed grains to enhance mechanical properties. It is important to note that MEX and MIM metals do not experience textural bias resulting from multiple layers of rapidly cooling material, though MEX metals can still exhibit anisotropy due to the directional nature of the extrusion process.[17–19,21,33] DED and LPBF produce very high thermal gradients and cooling rates that can induce significant tensile residual stresses at the surface of parts.[3,12] This degrades the mechanical properties of the material, especially the fatigue life. MIM and MEX metals do not experience such an extreme thermal gradient during sintering, meaning that residual stress is not usually as much of a problem. MIM and MEX techniques can experience grain coarsening if the sintering time or temperature gets too high, but this can be controlled by using fine alloy powders.[55] The microstructural morphology for each AM method can be complex and can depend on many factors such as build plate temperature, cooling rate, alloy purity, initial microstructure present, and powder size, among others.[3] For MIM and MEX metals, these critical factors are densification, alloy purity (including debinding effectiveness), sintering time, sintering temperature, cooling rate, and powder particle size.[56]

After sintering, the microstructure of the BMD samples is a relatively fine, equiaxed $\alpha - \beta$ structure as seen in **Fig. 7(a)**, but with a lower percentage of β between the α laths than in the as-received sheet (**Fig. 7(b)**). The as-received sheet had smaller, more consistently sized grains. The grains in the BMD samples were likely larger due to the high sintering temperature. When compared with four Ti64 micrographs from Tuncer et al. that show microstructures from four different peak sintering temperatures, the one that appears the most similar to the structure in the present work corresponds to a peak temperature of at least 1100°C, though this is not certain. German et al. state that typical Ti64 sintering temperatures range between 1200°C and 1400°C. Tuncer et al. note that a reaction between (Al_2O_3) and Ti is known to occur at elevated temperatures around 1150°C. Based on the high measured oxygen content in the samples and extreme discoloration on the surface that contacted the ceramic interlayer, it seems likely that this reaction did occur, potentially leading to brittle α-case formation.

The FT sheet that experienced the furnace conditions like the BMD samples had much coarser grains with more columnar α laths as seen in **Fig. 7(c)**. This is likely because the thermal

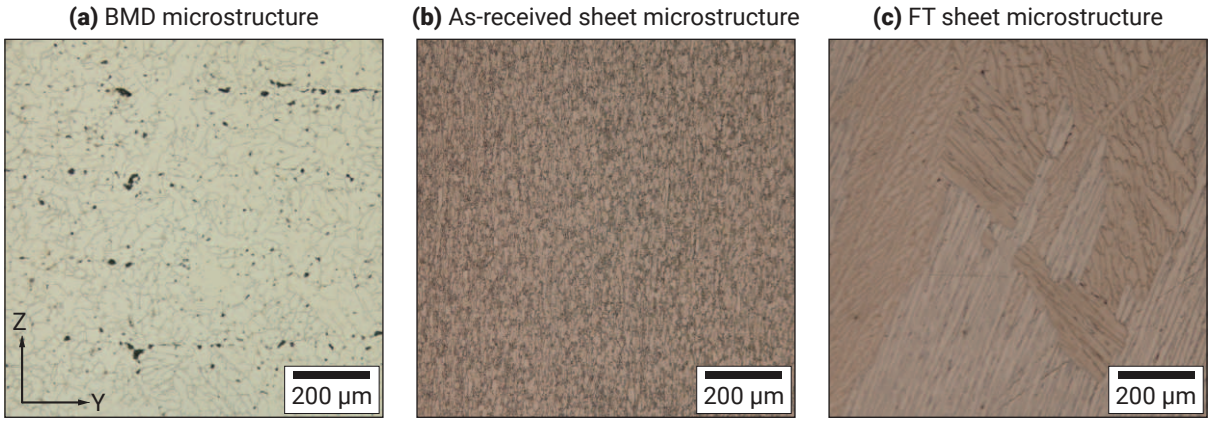

Fig. 7: *Polished and etched cross section of (a), the BMD microstructure showing a relatively fine, equiaxed grain structure with visible porosity and a high percentage of* α *phase, (b), the as-received sheet microstructure with a fine, equiaxed grain structure, and (c), the FT sheet microstructure with very coarse* α *laths.*

energy from what is essentially a recrystallization heat treatment, goes into growing and coarsening the grains through volume diffusion, rather than having to first dissolve thin oxide layers on the powder particles, commence surface diffusion between particles, and then start volume diffusion in the sintering process.[56] As discussed later, it is possible that the coarse microstructure and resulting high anisotropy leads to lower ductility and UTS in the FT sheet than in the as-received sheet.

3.4 Porosity

The percentages of the overall and the interlayer porosity of the samples are presented in **Fig. 8**, and tabulated data are in **Table S4**. The overall porosity for three BMD gauge cross section images was generally higher than the interlayer porosity taken from cropped images in between the lack-of-fusion porosity. In both sets of results, there is a high outlier at 2.41% for the overall porosity and 1.37% for the interlayer porosity. The 2.41% value is very close to the reported porosity from Desktop Metal of 2.5%, inferred from their reported 97.5% relative density.[66] The source of this data was published in 2024 in Tuncer et al.[27] The authors state that they achieved a relative density of 97.5% at 1130°C. They achieved a higher density of over 98% at 1200°C and higher but found that the Al_2O_3 interface material started reacting with the Ti64 and sticking to the part. To minimize this reaction, the Desktop Metal sintering cycle likely reaches about 1130°C for Ti64, though the reaction can still occur at temperatures reaching 1100°C and above, potentially allowing diffusion of oxygen and aluminum into the part regardless. In addition to reducing the surface roughness, the formation of brittle α-case titanium may have been one of the reasons for post-machining the samples in the study, which partially negates the net-shape benefit of AM.

Porosity values for Ti64 generally range from 0.09%–0.25%[67] for EBM-processed samples and around 0.08% for LPBF-processed samples.[68] The MIM literature reports relative density values between 94.5% and 99.5% with a mean of 96.8%, while MEX Ti literature reports values between 95.5% and 99.1% with a mean of 97.2%.[28,49,50,55] Thus, the average value of 1.52% porosity from this work which corresponds to a 98.48% density, is higher than Desktop

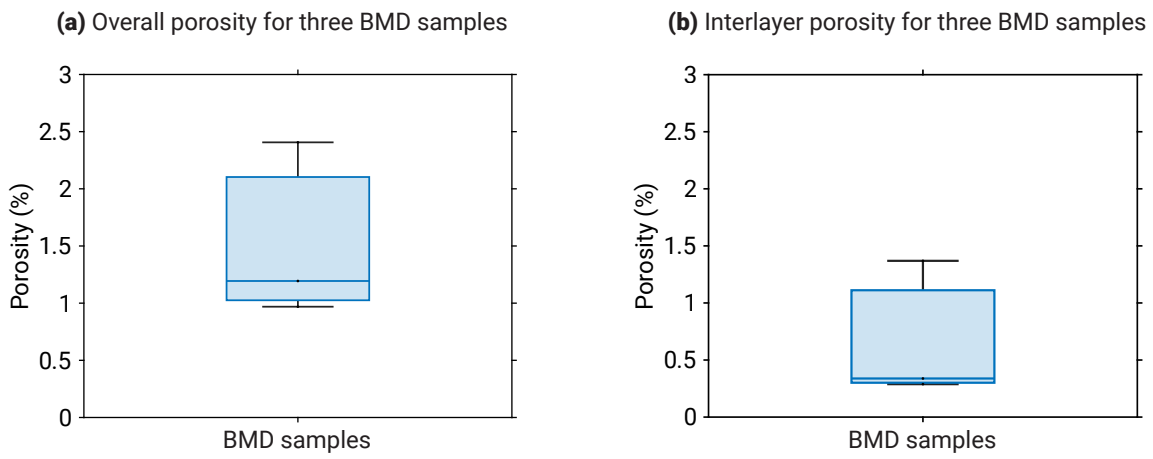

Fig. 8: *Percent porosity for three BMD samples calculated using optical images of polished cross sections via a custom MATLAB script. (a) Shows the overall porosities of the three cross section while (b) shows the smaller interlayer porosity present between the larger lack-of-fusion pores.*

Metal's reported value, and at the higher range of values reported by the MIM literature. The average difference between the overall porosity and the interlayer porosity was 0.86%, which indicates that more than half of the porosity volume is within the print layers, between the lack-of-fusion porosity. This is retained porosity from contaminant gas entrapment during the sintering process.

Because sintering is so important in the final properties of MIM and MEX metals, including porosity, it is valuable to briefly discuss this process. Densification is one of the most important factors for maintaining sufficient bulk mechanical properties. The most statistically significant factors for effective titanium alloy densification are small particle size, slower heating rate, and higher hold times.[56] Although the Desktop Metal furnace does not provide a temperature profile, this study found that the sintering time aligns with typical MIM and MEX processes reported in the literature. Typical hold times range between 120 and 240 min.[56] The sintering hold time for the samples in this work was about 240 min, within the common range. Alloying also tends to improve densification via an upward shift in the $\alpha - \beta$ transus temperature and through higher diffusion mobility through aluminum.[56] This makes Ti64 a good candidate for sintering, though a major factor that can decrease the quality of the material and inhibit densification is the introduction of impurities during the sintering process that reduces ductility and induces retained porosity.[56]

High porosity resulting from incomplete densification can be detrimental to the overall properties of the final part. Thus, pore filling is critical during sintering. The pore spaces can be thought of as large vacancies in the crystallographic structure, allowing them to be filled via volume diffusion.[56] However, filling reaches a limit as gas pressure from impurities in the material builds within the pores. When this internal pressure exceeds the pore-filling capillary pressure, the pore can no longer continue to shrink, leading to retained porosity.[56] At this time, pores stop closing, densification comes to a halt, and the retained pores tend to grow as the temperature remains elevated, making it important not to over-sinter.[56] Porosity in MIM Ti alloys is known to reduce its strength and stiffness, and in fact, this is sometimes the goal, such as for biomedical implants.[69]

In applications where maximum strength and stiffness is required, this is not desirable. Though porosity generally decreases the strength and stiffness of AM metals, the porosity observed here may not be enough on its own to account for the low strength and very low ductility observed in the samples. It is likely one of several factors that affect the strength and ductility. The porosity values in this work indicate effective sintering and pore filling via a combination of small powder particles (around 20µm in diameter), slow heating rate, and a high hold time of about 240 min. As noted previously, the maximum temperature likely reached at least 1100°C, though it could have been as high as 1200°C to 1300°C.[27] Due to the high contamination content, which inhibits pore filling, the porosity was expected to be lower due to retained contaminant gases within pores. It is possible that these contaminants diffused interstitially into the material, rather than remaining in the pores. Regardless, the porosity values observed in this work, are similar to the literature values for MIM and MEX which achieved much higher elongations and ultimate strengths.[27,50,55] While the observed porosity of this work does reduce the strength and ductility of the samples, other factors such as α-case formation and high surface roughness likely contribute more to the extreme reduction in properties, as will be discussed in the following sections.

3.5 Mechanical Testing

Hardness Testing

In the first portion of hardness testing, Knoop microhardness tests were conducted on two BMD samples, two FT sheet samples, and one as-received sheet sample at five locations on the surface of the polished cross sections: bottom, left, middle, right, and top. **Fig. 9** shows data for each sample condition, and **Table S5** and **Table S6** contain tabulated statistical data for two total samples in each condition. Images of the indented samples are shown in **Fig. S2**. The Knoop hardness of grade 5 titanium in the annealed condition is around 36 HRC[70] which converts to

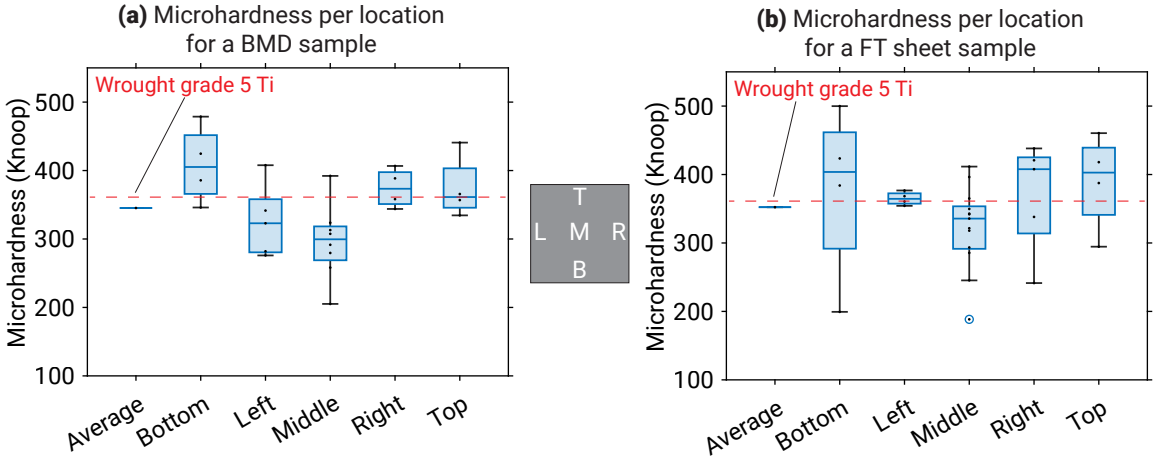

Fig. 9: *Data showing Knoop microhardness values for five sample locations labeled bottom, left, middle, right, and top. Every hardness measurement was averaged and is listed on the plot. (a) The data for a BMD sample and (b), the data for the FT sheet sample. Data is relatively consistent, though the middle sections of both specimens had the lowest mean hardness, and the bottom of the BMD sample had the highest hardness, perhaps due to Al_2O_3 contamination from the interface material.*

360 on the Knoop scale. The average measured Knoop hardness on the as-received sheet was exactly 360 averaged from 22 indentations. The average values for the BMD sample and the FT sheet samples were 345 and 352 Knoop, respectively, which are slightly lower than the typical grade 5 value. The hardness of the two samples was not much reduced when compared with the specification and may not be statistically significant since the mean falls within the middle two quartiles of most of the data. Notably, the hardness in the middle sections of the samples was generally lower, particularly in the BMD sample, which could indicate lower levels of diffused interstitial contamination. The middle 50% of data taken from the center of the BMD sample falls outside of the full range of data from the bottom, right, and top measurements in the same sample, indicating that the lower values taken from the middle of the sample are statistically lower. The higher local hardness at the edges could indicate oxygen, aluminum, or other contaminant introduced through the surface of the parts via the Al_2O_3 ceramic interface material and/or leakage into the furnace. Note that the ceramic interface surface (bottom) has the highest mean hardness. It was determined that more comprehensive testing was required to quantify if there were significant hardness changes through the depth of the material, due to α-case titanium formation.

In the hardness versus depth testing, **Fig. 10** shows a clear increase in hardness at the ceramic interlayer surface of the BMD samples near zero height up to about 549 Knoop and 448 Vickers. These are much higher than the average values for the entire sample, which were 385 Knoop and 358 Vickers, if the high outliers at the ceramic interface surface are removed. Note that the Vickers indentation could not get as close to the sample edge, resulting in a lower hardness than for the Knoop indentations. The higher hardness at zero depth continues through about 0.2 mm for the Knoop data and at least through 0.15 mm for the Vickers data indicating a significant

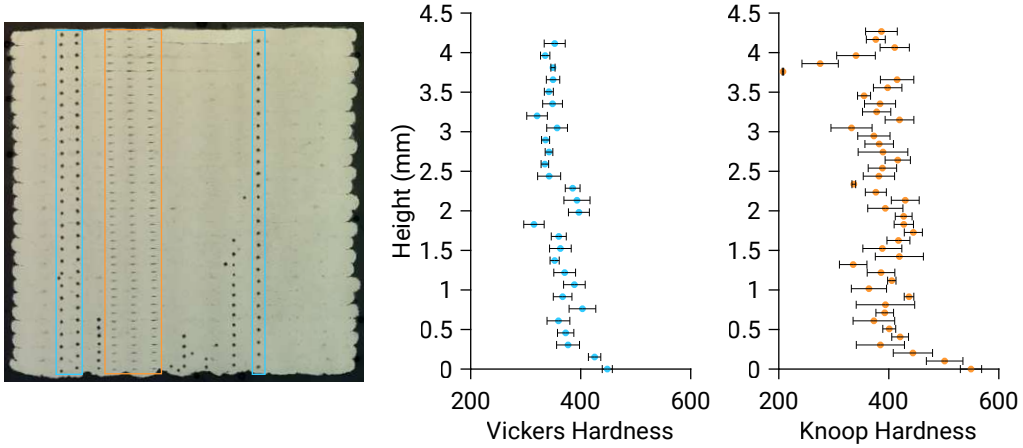

Fig. 10: *Knoop and Vickers hardness measurements beginning at the bottom of the BMD sample (ceramic interlayer surface) and progressing upward. Three measurements were taken at each depth for both the Knoop and the Vickers measurements. Higher hardness at the ceramic interlayer surface indicates the presence of α-case titanium. The Knoop measurements could be taken closer to the sample edge due to the lower indentation volume, and, therefore, could read higher hardness values closer to the surface than the Vickers indenter could. The error bars represent the standard error of the three measurements taken at each depth.*

formation of α-case through that depth. Note that no increase in hardness is observed at the top of the sample. This suggests that α-case titanium formed at the ceramic interlayer surface due to Al_2O_3 contamination, but was likely not present to a significant degree on the other surfaces of the part due to the sintering atmosphere.

Fig. 11(a) shows the Knoop and Vickers indentations for the sample along with an etched image of the sample cross section overlaid with an image of the indented surface. The average Knoop hardness in the vertical direction was 467 and the average hardness in the horizontal direction was 446. The average Vickers hardness in the vertical direction was 363 and the average horizontal hardness was 409. The hardness of the FT sheet was higher than expected for such coarse grains and thick laths as seen in **Fig. 11(b)** and **(c)**. The orientation of large oriented α lath colonies played a large role in the measured hardness. Many of the α colonies visible in the sample are oriented such that the laths run longitudinally in plane with the polished cross section as seen in **Fig. 11(d)** and **(f)**. The closer this angle is to parallel with the polished plane, the higher the measured hardness value. The laths oriented in this direction could be hindering dislocation movement more effectively and causing high dislocation densities. Further analysis is required to determine the exact cause. While interesting, this is not the main focus of this study, rather, the properties and failure mode of the BMD samples are the main focus. As the angle shifts so that the laths run perpendicular to the polished cross section (or nearly so) as seen in **Fig. 11(e)** and **(g)**, the hardness decreases toward the typical hardness of a fine-grained Ti64 sheet. The high average hardness values in the FT sheet sample may be the result of a large number of α colonies oriented at or near parallel with the polished cross section plane. During cooling, it is possible that many of these neighboring colonies formed in similar orientations with only slight angular mismatches between them, resulting in a high anisotropy in local regions of the sample cross section. However, another competing α colony with a much different orientation could dominate in another portion of the sample. Any laths that had a high angular mismatch would have much different hardness values.

Fig. 11(d)–(g) show how the orientation of the laths influence the hardness measurements with the longitudinal orientation resulting in higher hardness and the transverse orientation resulting in lower hardness. If a large number of the colonies are oriented in a longitudinal direction (or nearly so) with respect to the polished cross-sectional plane, then this could explain the high average hardness values observed in the samples. However, even in colonies aligned in the transverse direction, the hardness was still higher than what might be expected by the Hall-Petch relation.[71] Two possible explanations are given, though without further testing, they are just conjecture. First, this could be the result of strain hardening. No twins could be observed in the microstructure to indicate strain hardening by that mechanism, but another technique such as Transmission Electron Microscopy (TEM) would be needed to observe dislocation densities and whether strain hardening took place. The second reason could be due to α-case formation. Though some of the hardness values are higher near the edges of the FT sheet sample where one might expect α-case to form, some of the values are equally high near the center due to the presence of the longitudinally oriented laths in those locations.

The high hardness throughout the sample cross section could indicate a more complete diffusion of oxygen throughout the depth of the part and could further explain the brittle fracture

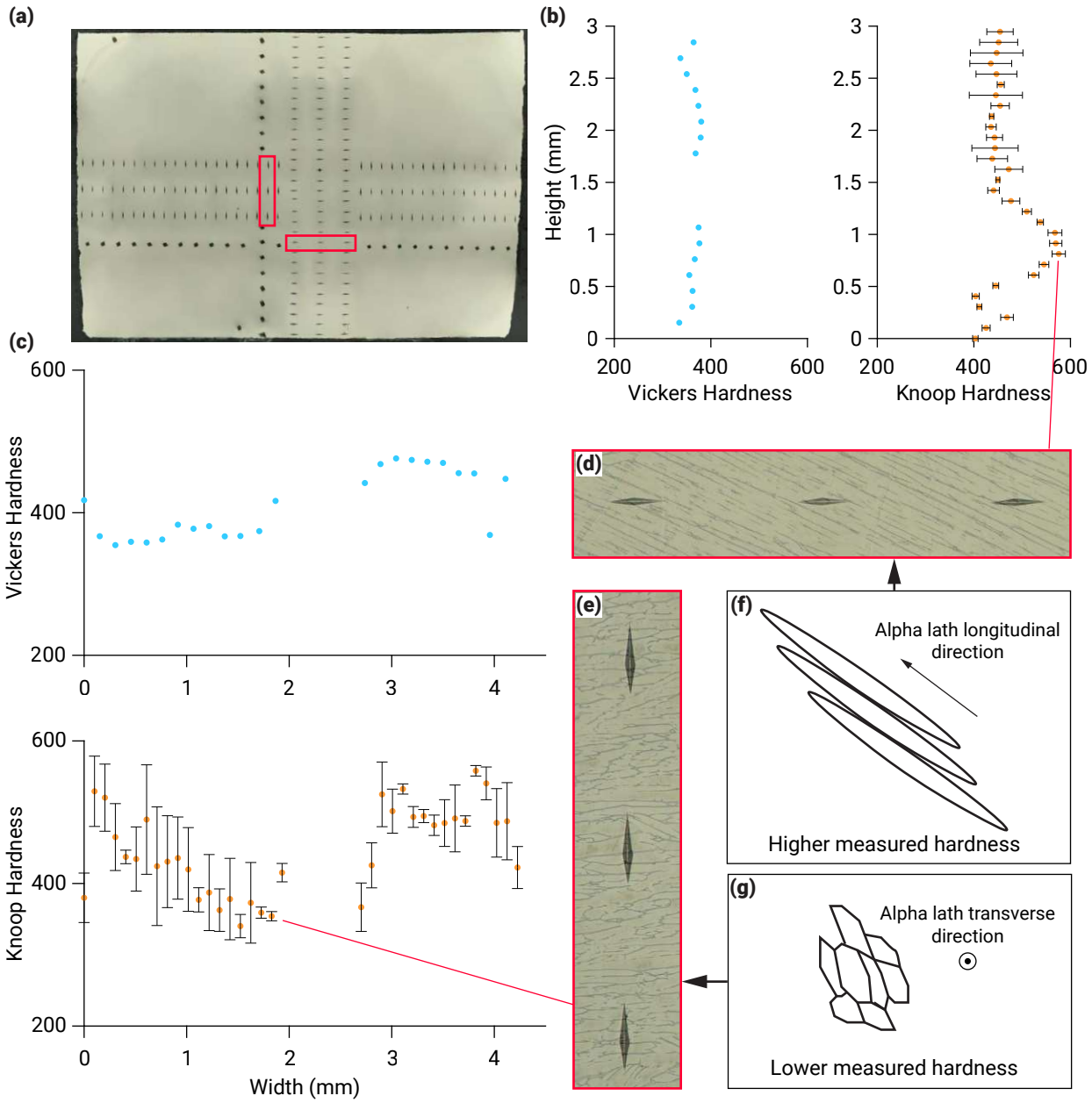

Fig. 11: *(a) A stitched image of Knoop and Vickers hardness indentations along the horizontal and vertical directions of the FT sheet sample. (b) Hardness data in the vertical direction and (c), hardness data in the horizontal direction. Three measurements were taken and averaged at each depth for the Knoop measurements. One measurement was taken at each depth for the Vickers measurements. (d) A magnified view of an area of high hardness that corresponds with α laths oriented in the longitudinal direction with respect to the sample cross section and (e), which shows a magnified view of an area of low hardness that corresponds with laths oriented transversely with respect to the sample cross section. Simplified illustrations in (f) and (g) show the α lath orientations. The error bars represent the standard error of the three measurements taken at each depth.*

observed during tensile testing. The complete diffusion may have occurred in the FT sheet samples and not in the BMD samples because oxygen could immediately begin diffusing into them, without having to use energy to sinter the material like in the BMD samples. Although elevated levels of oxygen were present in the FT sheet samples, further analysis would be required to verify the presence of α-case.

Overall, this leads to the conclusion that the ceramic interlayer material caused the formation of α-case and is the primary reason for the higher hardness in the BMD sample at the ceramic interlayer surface, which is the main focus of this work. It cannot be conclusively shown that there is any α-case formation on the FT sheet samples, though there is a high sensitivity of hardness to α lath texture.

Tensile Testing

Tensile tests for 12 BMD samples are reported in **Fig. 12(a1)**. The statistical data for UTS is reported in **Fig. 12(a2)** and the data for strain to failure is reported in **Fig. 12(a3)**. The most obvious result is the very low mean strain to failure of 0.65% observed in these tests. The mean UTS of 655 MPa is generally lower than other MIM and AM data as well.

A recent review paper by Nguyen et al. compiles the properties of Ti64 produced via various methods.[3] The UTS for Ti64 produced with electron beam PBF ranges from about 790 MPa at the lowest up to 1116 MPa with elongations ranging from 2.2% to 13.7%.[3] For DED, the UTS ranges from 881 MPa to 1103 MPa with elongation values ranging from 3% to 19%. For laser based PBF, values range from 945 MPa to 1421 MPa with elongation values from 1.4% to 19%.[3,72] For comparison, a typical wrought value is 993 MPa[70] but it can range from 870 MPa to 1030 MPa, with elongation between 4.5% and 20%, highlighting the higher UTS values possible with AM.[3] While many of these data points represent as-built samples, some underwent heat treatment, annealing, stress relief, or hot isostatic pressing.[3]

The MEX (including BMD) process is actually more similar to (MIM) than it is to direct AM methods, which means that it is more comparable to look at MIM properties in Ti64 for expected process-structure-property (PSP) relationships in Ti64 processed with BMD, though direct AM is still a good benchmark for comparison. Desktop Metal reports a UTS of 845 MPa and an elongation of 17% for their Ti64 alloy.[66] Two review papers, by Dehghan-Manshadi et al. and Suwanpreecha and Manonukul, report on the properties of MIM and MEX Ti64, citing UTS values between 749 MPa and 925 MPa with a mean of 836 MPa and elongation values between 3.8% and 18% with a mean of 12.2%.[28,49,50,55] The same sources report MEX UTS values between 875 MPa and 1000 MPa with a mean of 939 MPa, and elongation values between 3.4% and 18.5% with a mean of 11.8%.[28,49,50,55] Tuncer et al. used the Studio System 2 to produce Ti64 tensile dogbones.[27] They machined them after printing, which may contribute to increased ductility compared to the as-built condition tested in the present work. They sintered samples between 1050°C and 1300°C and obtained average UTS values between 810 MPa and 925 MPa with the strength generally increasing with increased sintering temperature. The elongation values did not increase linearly with temperature. It appeared more random, with average values ranging between 5% and 20%. However, there were a few outliers in the 1050°C and the 1150°C cases that had less than 2.5% elongation. The values that Desktop Metal reports in their product data

sheet appear to be on par with these MIM and MEX literature values, though direct AM methods are generally higher. Overall, compared with typical wrought values, the average UTS of the present work was lower by 34% and the elongation was reduced by more than an order of magnitude. Compared with typical MIM and MEX values, the UTS was lower by about 25%. Thus, substantial process refinement and post-machining would be necessary for this material to be viable in applications that typically utilize AM or MIM Ti64.

Fig. 12(b1) shows how lower stress generally corresponded with lower strain in these samples. As noted above, high oxygen or other α stabilizers usually results in lower ductility and higher strength. A work by F.H. Froes provides a graph of elongation to failure vs oxygen contamination.[73] Based on the plot, as oxygen contamination exceeds 0.4 wt%, the elongation drops below 5%. Although beyond the range of the graph, this implies that even higher oxygen percentages could cause even lower elongation. The measured oxygen in the two BMD samples in this work ranged from 0.30 to 0.39 wt%, and the O_{eq} ranged from 0.413 to 0.510 wt%, but this is an average value for a portion of the sample. It is possible that an area of high local contamination could cause even more extreme brittleness.

The high surface roughness also reduces the elongation in AM parts, although not normally as much as was observed in this work.[58,74,75] The α-case titanium formation paired with high surface roughness, especially at the ceramic interlayer face, causes a starker reduction in the total elongation than either one alone. As observed in Formanoir et al., a high surface roughness in a part actually reduces the load-bearing area of the sample cross section.[58] Since the samples in this study were measured with calipers, the cross-sectional areas were calculated using the maximum distance between the highest ridges on the sample surface, and not from the defects closest to the interior. Calculating UTS based on a corrected, reduced cross-sectional area would yield a higher value, although it could still be lower than typical MIM and MEX values. Thus, any strengthening of the material that occurs through α stabilization is offset by the premature cracking caused by α-case and high surface roughness. As seen later in the fractography data, cracks likely nucleate from the rough ceramic interface surface and induce instantaneous brittle fracture.

Also seen in **Fig. 12(b1)** and **(b2)**, is how the furnace level and position seemed to have played a role in the mechanical properties due to contamination from system leakage during sintering. The UHPA flows upward from the first level to the fourth level as shown in **Fig. 12(b2)**. This gas may carry leaked gaseous impurities that could result in non-uniform specimen exposure to the leaked air, as the closer specimens act as getters. Additionally, specimen position could also play a role, as Position 1 and 2 are closer to the gas outlet than Position 3 and 4. Based on the results in **Fig. 12(b1)**, it is possible that lower furnace level and lower furnace position may cause a reduction in UTS and elongation to failure in the samples, though even the samples further from the gas flow still had very low values. Thus, the potential leakage could have a significant influence on the contamination level in the samples, and the furnace atmosphere may not be sufficient at shielding. Additionally, the roughing pump on the furnace may not reach low enough pressures to adequately control contamination either. Desktop Metal has recently introduced a new furnace which includes a higher vacuum turbo-pump, potentially for this reason.

Fig. 13 shows the DIC strain fields at five strain points overlaid onto three samples, one in

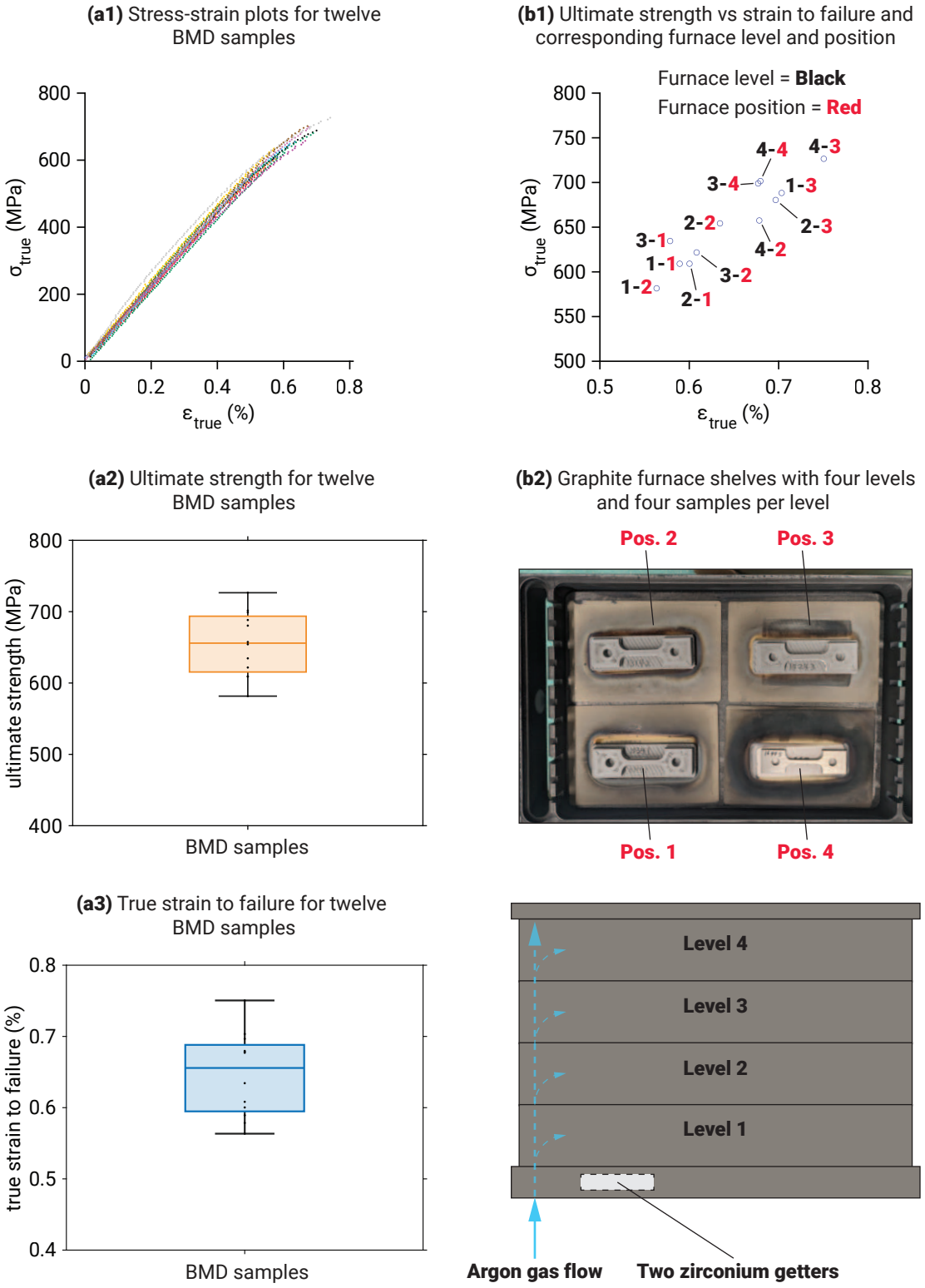

Fig. 12: *(a1) Stress-strain curves that show consistent low ductility, (a2) the UTS for the samples with a mean of 655 MPa, and (a3), the strain to failure for the samples with a mean of 0.65%. (b1) A plot that shows how lower furnace level and position may correspond to reduced UTS and strain to failure. (b2) A diagram of furnace shelf level and sample position during sintering.*

(a) DIC strain field of BMD sample at incremental strain values and corresponding stress-strain curve

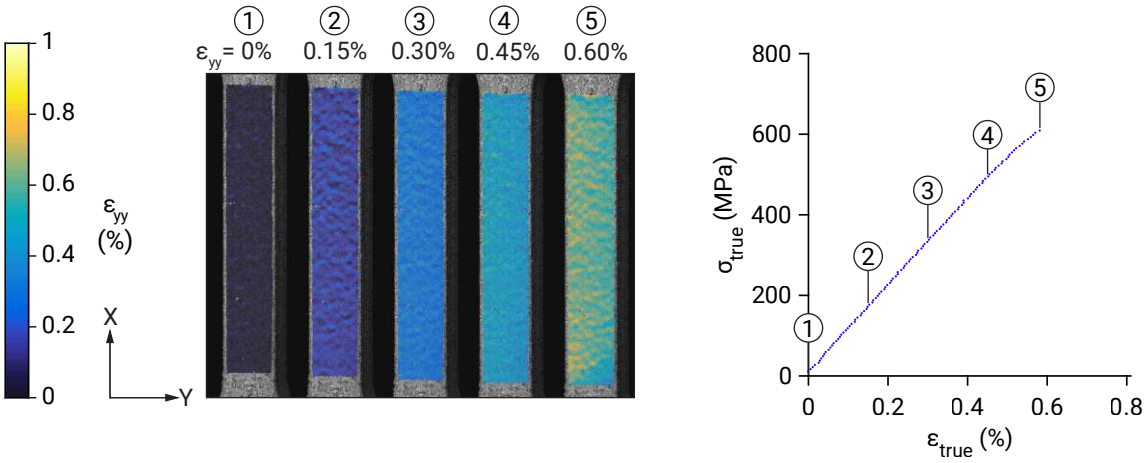

(b) DIC strain field of FT sheet sample at incremental strain values and corresponding stress-strain curve

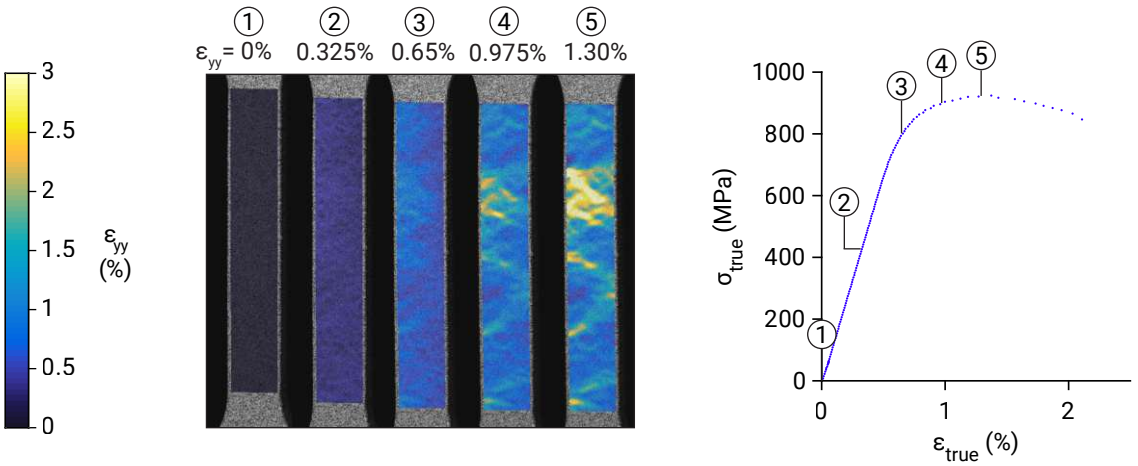

(c) DIC strain field of as-recieved sheet sample at incremental strain values and corresponding stress-strain curve

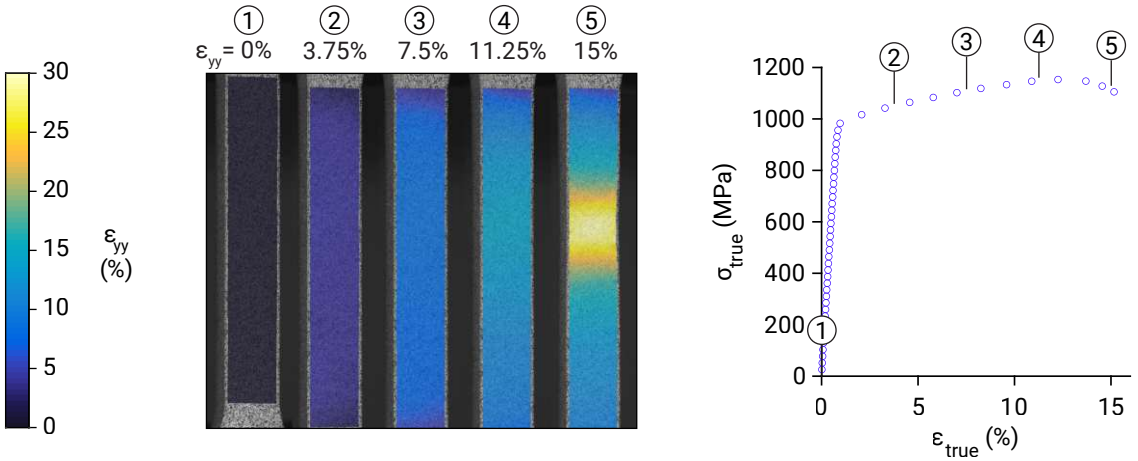

Fig. 13: *DIC strain fields at incremental strain values and corresponding stress-strain curves for (a), a BMD sample showing directional localization on ±45° planes, (b), an FT sheet which shows coarse localization along ±45° planes, and (c), an as-received sheet which does not show visible ±45° localization due to a very fine grain microstructure.*

each of the conditions tested. It also includes the corresponding stress-strain curve with numbered labels with the same strain values as the strain field overlays. Note that the image overlays report the average ε_{yy} value for the entire overlay area, while the stress-strain curves report ε_{true}. While these values are similar, they are not exactly the same, resulting in some small mismatch between the image and the plot. **Fig. 13(a)** shows a crossing $\pm 45^{\circ}$ pattern in the strain field in images 2–5, indicating localized strain. For example, in image 5, the yellow regions showing strains up to 1% are likely aligned with slip systems lined up preferentially with the loading direction. Several studies have indicated that local plastic slip tends to appear along grain boundaries aligned $\pm$ 45° with respect to the loading direction.[76,77] Regions where three grains come together (triple junctions) are more likely to form slip bands due to a higher chance of forming a preferentially oriented system than a single grain interior alone.[53,76,78,79] Intragranular slip can also cross grain boundaries to become intergranular slip if neighboring grains have similar textures and Schmid factors.[77,78,80] **Fig. 13(b)** for the FT sheet shows much coarser localization as expected, since the size of the grains in these samples was much larger. Large grains with roughly $\pm$ 45° orientation relative to the loading direction are likely to exhibit intragranular slip, as this orientation results in the highest shear stress. Additionally, large mismatches between neighboring lamellar structures will cause high local stress and strain along the prior beta grain boundaries, inducing premature brittle fracture.[81] This is indeed what is observed in the strain overlay of **Fig. 13(b)**. Any sufficiently large defect on the surface can induce the formation of a crack and initiate fracture. The fracture does indeed begin at the surface of the FT sheet sample where the highest local strain was observed as seen in **Fig. 13(b)**. Another work by Rani et al.[71] showed that an increase in heat treatment temperature and time caused a reduction in strength and ductility due to the increase in α lath thickness. That work observed about a 7.5% elongation for a lath thickness of 2.2μm. The lath thickness of the present work was on the order of 10 μm, which could further explain the low elongation of about 2% seen in **Fig. 13(b)**. However, Rani et al. also found a much reduced hardness in the coarse-grained, low ductility samples, unlike the FT sample in this work which showed increased hardness. Again, it could not be conclusively shown in this work, but α-case formation or strain hardening could be possible reasons.

In **Fig. 13(c)**, there is no macroscopic strain localization because the grains are too small for the resolution of the DIC cameras. With higher resolution imaging, similar $\pm$ 45° bands would be observed, albeit at a much smaller scale and with potentially more microscopic slip mechanisms at play. Because of the fine texture, the only visible, local strain band occurs in a direction normal to the loading direction where necking occurs. The elongation of 15% is typical for an annealed Ti64 sheet.

3.6 Fractography

The fracture surface of a sample from each condition was imaged using SEM to determine the mechanisms of failure for each. **Fig. 14(a)** shows an image of the entire BMD fracture surface in the center of the figure with two magnified insets. **Fig. 14(b)** shows a magnified view of an area near the center of the sample cross section, highlighting features indicative of mixed-mode cleavage, dimple rupture, and brittle intergranular decohesion fracture.[82] Porosity can clearly be observed, contributing to the fracture. To fully isolate the effects of porosity on the samples, other tests would need to be conducted, such as tensile testing on BMD samples with smooth,

post-machined surfaces and/or no α-case present. Larger pores that are surrounded by several grains likely contribute to intergranular fracture, while smaller pores within grains likely contribute to transgranular dimple rupture. **Fig. 14(c)** shows a larger area of the likely fracture initiation site, as evidenced by the striations originating from a particularly rough portion of the

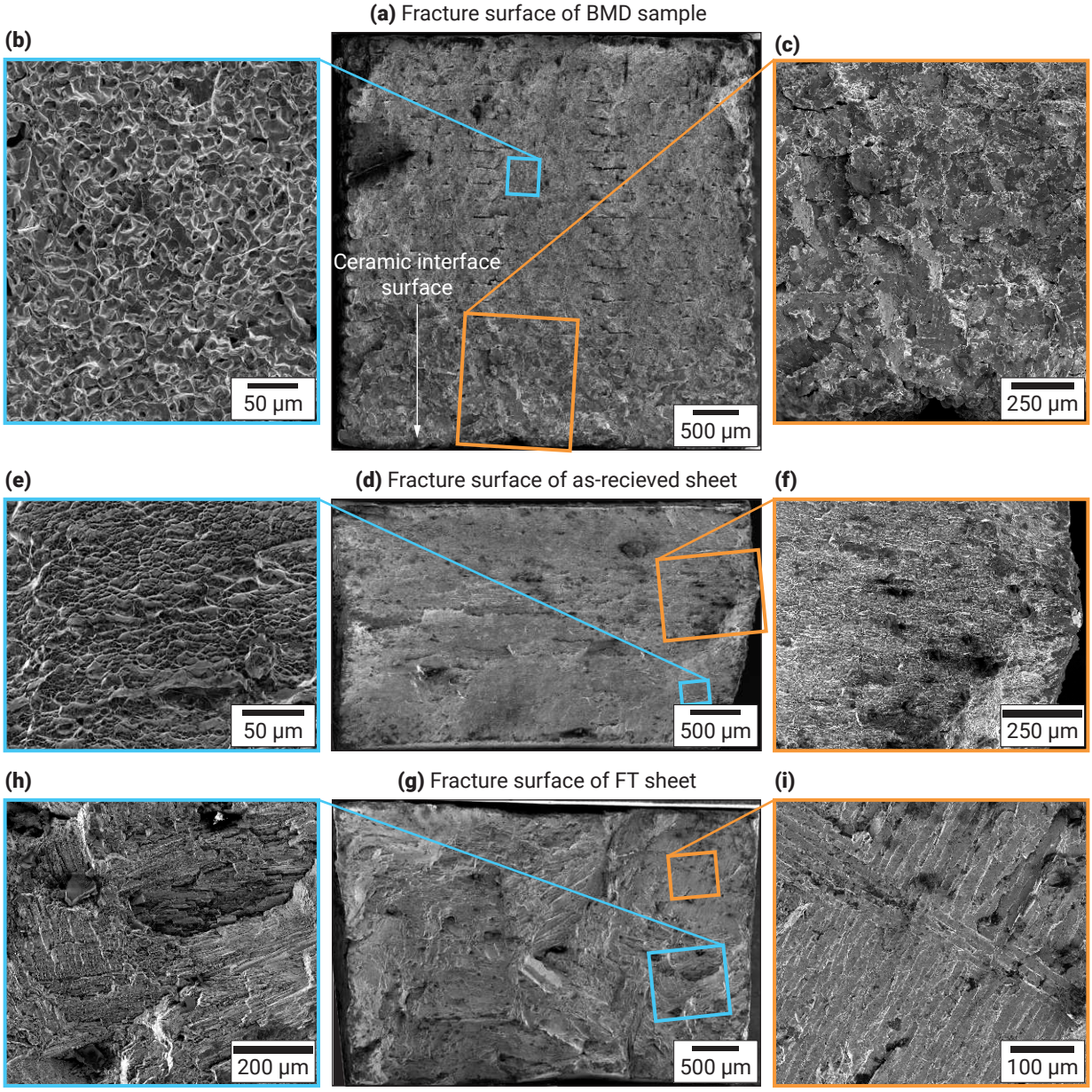

Fig. 14: *(a) Fracture surface of a BMD sample showing a magnified view of (b), dimple rupture, brittle intergranular decohesion, and (c), brittle quasi-cleavage fracture where the fracture likely initiated. (d) Fracture surface of an as-received sheet sample showing (e), non-uniform cups from dimple rupture and (f), the likely fracture initiation site. (g) Fracture surface of a furnace treated sample showing (h), very coarse intergranular fracture and (i), the known fracture initiation site with the characteristics of a classic brittle cleavage fracture through a single grain.*

sample surface where there are some unmelted powder particles. This area displays predominantly cleavage morphology that is mixed with small areas of decohesion and dimple rupture, similar to what is seen in **Fig. 14(b)**. Both the decohesion and cleavage fracture modes are indicative of brittle fracture. Of particular importance is that the entire southern portion of the fracture surface displays this cleavage morphology, perhaps indicating the presence of α-case titanium. All other BMD samples that were tensile tested had this morphology in the southern region of the sample. This is the surface of the part that rested on the Al_2O_3 ceramic interlayer. It is likely that oxygen contributes to brittle cleavage through the α-case formed at this surface, as evidenced by hardness testing. It is known that α-case titanium formation at the surface of parts leads to low ductility and early crack nucleation.[1] After the crack initiation at this surface, the samples failed in an instantaneous manner via decohesion and cleavage. The apparent dimple rupture morphology, which is normally ductile in nature, did not appear to indicate ductility in the part. Perhaps the severe contamination on the surface or surface roughness negated any benefits from ductility on the interior. It is also possible that this morphology, while appearing like dimple rupture could be purely intergranular decohesion.

The fracture surface of the as-received sheet is shown in **Fig. 14(d)**. **Fig. 14(e)** clearly shows classic dimple rupture caused by microvoid coalescence.[4,82] This mode of failure is expected and common in Ti64. It is probable that the fracture initiated in the region of **Fig. 14(f)**. Perhaps there was a small surface defect that concentrated the stress enough to cause the failure to start there. What is not apparent from the image is that this fracture surface protrudes at a $\pm 45^\circ$ angle and comes to a sharp point. As discussed earlier, this occurs because the shear stress is maximized in the $\pm 45^\circ$ direction, leading to slip occurring through the grains and grain boundaries oriented in that direction.

Fig. 14(g) shows the fracture surface of the FT sheet sample. **Fig. 14(h)** shows a very coarse intergranular fracture paired with large cleavage facets due to the very large grains observed earlier. Some areas on the surface not shown in high magnification have some dimple rupture morphology indicated by cupping, suggesting some level of ductility. The observed elongation value of about 2.2% in this sample as seen in **Fig. 13(b)** indeed provides clear evidence for more ductility than what was observed in the BMD samples, though it is still much lower than the as-received sheet. The sample has a mixed mode fracture consisting of cleavage, intergranular decohesion, and small amounts of dimple rupture. **Fig. 14(i)** shows the region of known fracture initiation, where the crack was observed for several seconds during DIC acquisition. The location of fracture can be seen in the strain field of **Fig. 13(b)** at the region of highest local stress on the left edge of the sample. This region of the sample corner clearly experienced cleavage fracture through a single grain which morphs into the intergranular, cleavage, and dimple rupture mixed fracture rather abruptly. It is possible that this grain was aligned at nearly $\pm 45^\circ$ and had enough of a surface defect to cause fracture initiation. When the mismatch caused by misaligned coarse α lath colonies caused a high enough local strain to induce significant slip, the sample fractured in an intergranular manner.

4. Summary and conclusions

The microstructure and mechanical properties of a Ti64 alloy produced via the BMD print, debind, and sinter process was characterized via compositional analysis to determine contamination levels, metallography and microscopy to observe the structures of the parts, porosity analysis to evaluate the efficiency of the sintering densification process, hardness and tensile testing to provide basic mechanical properties, and fractography to provide insight into the fracture mechanisms involved. All BMD samples in this work followed the manufacturer-supplied procedures. BMD sample properties and microstructure were compared with conventional grade 5 titanium sheet, and grade 5 titanium sheet processed in the same furnace sintering cycle ("FT sheet"), to compare the effect of the heat treatment on wrought Ti64.

Key observations and conclusions of this work are:

1. The BMD samples produced in this work experienced a mass reduction of 6% between the green and brown state, and a mass reduction of 4.4% between the brown and sintered state, for a total 9.7% mass reduction.
2. The BMD samples experienced a shrinkage of 12.0% in the X, 12.4% in the Y, and 18.0% in the Z direction for an average 14.1% reduction in volume during processing.
3. The overall porosity for three BMD samples was measured to be 1.52% on average, which falls within the typical range of values for MIM Ti64 in the literature but could still reduce the strength and ductility of the parts.
4. For the BMD sample, the hardness increased from an interior bulk average of 358 Vickers to 448 Vickers at the ceramic interface surface and from a bulk average of 385 Knoop to 549 Knoop at the interface surface, indicating the formation of α-case titanium found to have penetrated to a depth of about 0.2 mm as seen in **Fig. 10**.
5. For the BMD samples, high levels of oxygen above ASTM B265 from the Al_2O_3 interlayer, the sintering atmosphere, high levels of carbon (at the specification threshold) from the binder, and potentially high levels of aluminum from the Al_2O_3, stabilized the α phase and led to the formation of α-case titanium (from oxygen) on the surface of the part that contacted the Al_2O_3 ceramic interface material. This brittle α-case formation in combination with high surface roughness at the ceramic interface surface and internal porosity, led to early crack nucleation and brittle cleavage and decohesion fracture with elongation more than 10 times lower and UTS 34% lower than wrought Ti64. The sample position and level within the furnace may have played a role in changing contamination levels in the samples due to their differing distance from the UHPA flow/leak path.
6. For the FT sheet samples, the average hardness was elevated compared to wrought Ti64, at 391 Vickers and 456 Knoop, and the hardness was highly sensitive to α colony orientation in which laths oriented in the longitudinal direction had higher measured hardness. Potential reasons for the high hardness are strain hardening or highly diffused α-case formation.
7. For the FT sheet samples, the high temperature heat treatment and slow cooling rate led to extreme α colony growth with areas of large orientation mismatch between colonies. This caused high local strain in the samples at $\pm 45^\circ$ with respect to the loading direction which induced early crack nucleation via brittle cleavage fracture that morphed into decohesion fracture after the crack passed through the grain. Brittleness may have been further induced

by the presence of α-case titanium formed by the high levels of measured oxygen.

Overall, the low UTS and the very low strain to failure observed in the BMD samples was the result of the interaction between high contamination introduced during the BMD process which formed α-case titanium, high surface roughness, and porosity which caused premature crack nucleation and instantaneous part fracture. With the processing route presented here, BMD for Ti64 may not be suitable for some applications that demand high strength and ductility with minimal contaminant content, although with some process tuning and perhaps some minor post-machining, the method may be refined into a promising AM method for certain applications.

Author contributions

Credit authorship contribution statement

E. Devine: Conceptualization; Data curation; Formal analysis; Investigation; Methodology; Sample preparation; Software; Validation; Visualization; Writing – original draft; Writing – review & editing; **M. Lester**: Conceptualization; Data curation; Formal analysis; Investigation; Methodology; Sample preparation; Validation; Visualization; Writing – original draft; **T. McElroy**: Conceptualization; Investigation; Methodology; Sample preparation; Validation; Writing – review & editing; **T. Valenzuela**: Conceptualization; Formal analysis; Methodology; Software; Validation; **W. LePage**: Conceptualization; Formal analysis; Funding acquisition; Investigation; Validation; Data Curation; Methodology; Project administration; Resources; Software; Supervision; Writing – review and editing.

Conflict of interest

The authors declare that they have no known competing financial interests or personal relationships that could have appeared to influence the work reported in this paper.

Supplementary materials

Supplementary material associated with this article can be found, in the online version, at (we will add URL later, at the current time the supplementary material is attached).

Data availability

Data will be made available upon request.

References

[1] Lütjering G, Williams JC (2003) Titanium. Engineering Materials and Processes, Springer Berlin Heidelberg, Berlin, Heidelberg, doi:10.1007/978-3-540-71398-2

[2] Blakey-Milner B, Gradl P, Snedden G, Brooks M, Pitot J, Lopez E, Leary M, Berto F, Du Plessis A (2021) Metal additive manufacturing in aerospace: A review. Materials & Design 209:110008, doi:10.1016/j.matdes.2021.110008

[3] Nguyen HD, Pramanik A, Basak AK, Dong Y, Prakash C, Debnath S, Shankar S, Jawahir IS, Dixit S, Buddhi D (2022) A critical review on additive manufacturing of Ti-6Al-4V alloy: Microstructure and mechanical properties. Journal of Materials Research and Technology 18:4641–4661, doi:10.1016/j.jmrt.2022.04.055, publisher: Elsevier Editora Ltda

[4] Joshi VA (2006) Titanium alloys: an atlas of structures and fracture features. CRC/Taylor & Francis, Boca Raton, OCLC: ocm61247248

[5] Jamróz W, Szafraniec J, Kurek M, Jachowicz R (2018) 3D Printing in Pharmaceutical and Medical Applications – Recent Achievements and Challenges. Pharm Res 35(9):176, doi:10.1007/s11095-018-2454-x

[6] Pragana JP, Sampaio RF, Bragança IM, Silva CM, Martins PA (2021) Hybrid metal additive manufacturing: A state–of–the-art review. Advances in Industrial and Manufacturing Engineering 2, doi:10.1016/j.aime.2021.100032, publisher: Elsevier B.V.

[7] Armstrong M, Mehrabi H, Naveed N (2022) An overview of modern metal additive manufacturing technology. Journal of Manufacturing Processes 84:1001–1029, doi:10.1016/j.jmapro.2022.10.060, publisher: Elsevier Ltd

[8] Rouf S, Malik A, Singh N, Raina A, Naveed N, Siddiqui MIH, Haq MIU (2022) Additive manufacturing technologies: Industrial and medical applications. Sustainable Operations and Computers 3:258–274, doi:10.1016/j.susoc.2022.05.001, publisher: KeAi Communications Co.

[9] Dutta B, Froes FH (2016) Additive manufacturing of titanium alloys: state of the art, challenges and opportunities. Joe Hayton, ISBN: 978-0-12-804782-8

[10] Brunette DM, Tengvall P, Textor M, Thomsen P (2001) Titanium in Medicine: Material Science, Surface Science, Engineering, Biological Responses and Medical Applications. Engineering Materials, Springer Berlin Heidelberg, Berlin, Heidelberg, doi:10.1007/978-3-642-56486-4

[11] Song B, Zhao X, Li S, Han C, Wei Q, Wen S, Liu J, Shi Y (2015) Differences in microstructure and properties between selective laser melting and traditional manufacturing for fabrication of metal parts: A review. Frontiers of Mechanical Engineering 10(2):111–125, doi:10.1007/s11465-015-0341-2, publisher: Higher Education Press

[12] Ye C, Zhang C, Zhao J, Dong Y (2021) Effects of Post-processing on the Surface Finish, Porosity, Residual Stresses, and Fatigue Performance of Additive Manufactured Metals: A Review. Journal of Materials Engineering and Performance 30(9):6407–6425, doi:10.1007/s11665-021-06021-7, publisher: Springer

[13] International Organization for Standardization (2021), *ISO/ASTM 52900: Additive manufacturing — General principles — Fundamentals and vocabulary (2nd ed.)*

[14] Montero J, Vitale P, Weber S, Bleckmann M, Paetzold K (2020) Indirect Additive Manufacturing of resin components using polyvinyl alcohol sacrificial moulds. In Procedia CIRP, vol. 91, 388–395, Elsevier B.V., doi:10.1016/j.procir.2020.02.191, ISSN: 22128271

[15] Akessa AD, Tucho WM, Lemu HG, Grønsund J (2022) Investigations of the microstructure and mechanical properties of 17-4 PH ss printed using a MarkForged Metal X. Materials 15(19):6898, doi:/10.3390/ma15196898
[16] Gonzalez-Gutierrez J, Cano S, Schuschnigg S, Kukla C, Sapkota J, Holzer C (2018) Additive manufacturing of metallic and ceramic components by the material extrusion of highly-filled polymers: A review and future perspectives. Materials 11(5), doi:10.3390/ma11050840, publisher: MDPI AG
[17] Chen R, Baich L, Lauer J, Senesky DG, Manogharan G (2022) Effects of Part Orientation, Printer Selection, and Infill Density on Mechanical Properties and Production Cost of 3D Printed Flexural Specimens. Manufacturing Letters 23:549–560, doi:10.1016/j.mfglet.2022.07.069
[18] Henry TC, Morales MA, Cole DP, Shumeyko CM, Riddick JC (2021) Mechanical behavior of 17-4 PH stainless steel processed by atomic diffusion additive manufacturing. The International Journal of Advanced Manufacturing Technology doi:10.1007/s00170-021-06785-1/Published
[19] Watson A, Belding J, Ellis BD (2020) Characterization of 17-4 PH Processed via Bound Metal Deposition (BMD). In Minerals, Metals and Materials Series, 205–216, Springer, doi:10.1007/978-3-030-36296-6_19, ISSN: 23671696
[20] Bose A, Reidy JP, Jorgensen L, Tuncer N (2023) Processing of Copper by Extrusion-based Additive Manufacturing. International Journal of Powder Metallurgy 59(1), ISSN: 0888-7462
[21] Caminero MA, Romero Gutiérrez A, Chacón JM, García-Plaza E, Núñez PJ (2022) Effects of fused filament fabrication parameters on the manufacturing of 316L stainless-steel components: geometric and mechanical properties. Rapid Prototyping Journal 28(10):2004–2026, doi:10.1108/RPJ-01-2022-0023, publisher: Emerald Publishing
[22] Benson J (2012) Safety considerations when handling metal powders. The Journal of The Southern African Institute of Mining and Metallurgy 112
[23] Graff P, Ståhlbom B, Nordenberg E, Graichen A, Johansson P, Karlsson H (2017) Evaluating Measuring Techniques for Occupational Exposure during Additive Manufacturing of Metals: A Pilot Study. J of Industrial Ecology 21(S1), doi:10.1111/jiec.12498
[24] Desktop Metal (2022), Materials by Type
[25] Chao M (2019) Fused-Filament Fabrication of Metal with a Markforged Metal X System. International Conference on Additive Manufacturing with Powder Metallurgy (AMPM2019)
[26] Forward AM (2024), Metal Filaments
[27] Nihan T, Reidy JP, Jorgensen L, Bose A (2024) Bound Metal Deposition of Ti-6AI-4V Alloy. International Journal of Powder Metallurgy 60(1)
[28] Singh P, Balla VK, Atre SV, German RM, Kate KH (2021) Factors affecting properties of Ti-6Al-4V alloy additive manufactured by metal fused filament fabrication. Powder Technology 386:9–19, doi:10.1016/j.powtec.2021.03.026
[29] Waalkes L, Längerich J, Imgrund P, Emmelmann C (2022) Piston-Based Material Extrusion of Ti-6Al-4V Feedstock for Complementary Use in Metal Injection Molding. Materials 15(1):351, doi:10.3390/ma15010351
[30] Liu B, Wang Y, Lin Z, Zhang T (2020) Creating metal parts by Fused Deposition Modeling and Sintering. Materials Letters 263, doi:10.1016/j.matlet.2019.127252, publisher: Elsevier B.V.
[31] Safka J, Ackermann M, Machacek J, Seidl M, Vele F, Truxova V (2020) Fabrication

Process and Basic Material Properties of the BASF Ultrafuse 316LX Material. MM Science Journal 2020(5):4216–4222, doi:10.17973/mmsj.2020_12_2020071, publisher: MM Publishing, s.r.o.
[32] Thompson Y, Gonzalez-Gutierrez J, Kukla C, Felfer P (2019) Fused filament fabrication, debinding and sintering as a low cost additive manufacturing method of 316L stainless steel. Additive Manufacturing 30, doi:10.1016/j.addma.2019.100861, publisher: Elsevier B.V.
[33] Gabilondo M, Cearsolo X, Arrue M, Castro F (2022) Influence of Build Orientation, Chamber Temperature and Infill Pattern on Mechanical Properties of 316L Parts Manufactured by Bound Metal Deposition. Materials 15(3), doi:10.3390/ma15031183, publisher: MDPI
[34] Galati M, Minetola P (2019) Analysis of Density, Roughness, and Accuracy of the Atomic Diffusion Additive Manufacturing (ADAM) Process for Metal Parts. Materials 12(24):4122, doi:10.3390/ma12244122, publisher: MDPI AG
[35] Gong H, Snelling D, Kardel K, Carrano A (2019) Comparison of Stainless Steel 316L Parts Made by FDM- and SLM-Based Additive Manufacturing Processes. JOM 71(3):880–885, doi:10.1007/s11837-018-3207-3
[36] Kurose T, Abe Y, Santos MV, Kanaya Y, Ishigami A, Tanaka S, Ito H (2020) Influence of the layer directions on the properties of 316l stainless steel parts fabricated through fused deposition of metals. Materials 13(11), doi:10.3390/ma13112493, publisher: MDPI AG
[37] Parenti P, Gavazzoni M, Foletti S, Colosimo BM (2025) Advancement on the small-scale fabrication of pure copper parts via material extrusion AM: process performance and quality mapping. Progress in Additive Manufacturing 1–29, doi:10.1007/s40964-025-00968-y
[38] Desktop Metal (2023), Maximum Studio System^{TM} Part Size
[39] Desktop Metal (2022), Studio System ^{TM} v.1 material process: print, debind, and sinter
[40] Desktop Metal (2022), Fabricate Desktop Parameter Settings
[41] Desktop Metal (2023), Best Practices for Part Placement in Furnace
[42] Follansbee P, Gray G (1989) An analysis of the low temperature, low and high strain-rate deformation of Ti-6Al-4V. Metallurgical Transactions A 20(5):863–874, doi:10.1007/BF02651653
[43] Chichili D, Ramesh K, Hemker K (1998) The high-strain-rate response of alpha-titanium: experiments, deformation mechanisms and modeling. Acta Materialia 46(3):1025–1043, doi:10.1016/S1359-6454(97)00287-5
[44] Nemat-Nasser S, Guo WG, Nesterenko VF, Indrakanti S, Gu YB (2001) Dynamic response of conventional and hot isostatically pressed Ti–6Al–4V alloys: experiments and modeling. Mechanics of Materials 33(8):425–439, doi:10.1016/S0167-6636(01)00063-1
[45] LePage WS, Daly SH, Shaw JA (2016) Cross Polarization for Improved Digital Image Correlation. Exp Mech 56(6):969–985, doi:10.1007/s11340-016-0129-2
[46] LePage W, Shaw J, Daly S (2017) Optimum Paint Sequence for Speckle Patterns in Digital Image Correlation. Exp Tech 41(5):557–563, doi:10.1007/s40799-017-0192-3
[47] Jones E, Iadicola M, Bigger R, Blaysat B, Boo C, Grewer M, Hu J, Jones A, Klein M, Lava P, Pankow M, Raghavan K, Reu P, Schmidt T, Siebert T, Simonsen M, Trim A, Turner D, Vieira A, Weikert T (2018) A Good Practices Guide for Digital Image Correlation. Tech. rep., International Digital Image Correlation Society, doi:10.32720/idics/gpg.ed1/print.format, edition: 1
[48] Tosto C, Tirillò J, Sarasini F, Cicala G (2021) Hybrid Metal/Polymer Filaments for Fused Filament Fabrication (FFF) to Print Metal Parts. Applied Sciences 11(4):1444,

doi:10.3390/app11041444
[49] Singh P, Balla VK, Gokce A, Atre SV, Kate KH (2021) Additive manufacturing of Ti-6Al-4V alloy by metal fused filament fabrication (MF3): producing parts comparable to that of metal injection molding. Prog Addit Manuf 6(4):593–606, doi:10.1007/s40964-021-00167-5
[50] Suwanpreecha C, Manonukul A (2022) A Review on Material Extrusion Additive Manufacturing of Metal and How It Compares with Metal Injection Moulding. Metals 12(3):429, doi:10.3390/met12030429
[51] Wen G, Cao P, Gabbitas B, Zhang D, Edmonds N (2013) Development and Design of Binder Systems for Titanium Metal Injection Molding: An Overview. Metall Mater Trans A 44(3):1530–1547, doi:10.1007/s11661-012-1485-x
[52] Dietrich K, Diller J, Dubiez-Le Goff S, Bauer D, Forêt P, Witt G (2020) The influence of oxygen on the chemical composition and mechanical properties of Ti-6Al-4V during laser powder bed fusion (L-PBF). Additive Manufacturing 32:100980, doi:10.1016/j.addma.2019.100980
[53] Delaire F, Raphanel J, Rey C (2000) Plastic heterogeneities of a copper multicrystal deformed in uniaxial tension: experimental study and finite element simulations. Acta Materialia 48(5):1075–1087, doi:10.1016/S1359-6454(99)00408-5
[54] ASTM (2020), ASTM B265-20a: Standard Specification for Titanium and Titanium Alloy Strip, Sheet, and Plate
[55] Dehghan-Manshadi A, Bermingham M, Dargusch M, StJohn D, Qian M (2017) Metal injection moulding of titanium and titanium alloys: Challenges and recent development. Powder Technology 319:289–301, doi:10.1016/j.powtec.2017.06.053
[56] German RM (2020) Titanium sintering science: A review of atomic events during densification. International Journal of Refractory Metals and Hard Materials 89:105214, doi:10.1016/j.ijrmhm.2020.105214, publisher: Elsevier BV
[57] Carroll BE, Palmer TA, Beese AM (2015) Anisotropic tensile behavior of Ti–6Al–4V components fabricated with directed energy deposition additive manufacturing. Acta Materialia 87:309–320, doi:10.1016/j.actamat.2014.12.054
[58] de Formanoir C, Michotte S, Rigo O, Germain L, Godet S (2016) Electron beam melted Ti-6Al-4V: Microstructure, texture and mechanical behavior of the as-built and heat-treated material. Materials Science and Engineering A 652:105–119, doi:10.1016/j.msea.2015.11.052, publisher: Elsevier Ltd
[59] Al-Bermani SS, Blackmore ML, Zhang W, Todd I (2010) The origin of microstructural diversity, texture, and mechanical properties in electron beam melted Ti-6Al-4V. Metallurgical and Materials Transactions A: Physical Metallurgy and Materials Science 41(13):3422–3434, doi:10.1007/s11661-010-0397-x
[60] Liu S, Shin YC (2019) Additive manufacturing of Ti6Al4V alloy: A review. Materials and Design 164, doi:10.1016/j.matdes.2018.107552, publisher: Elsevier Ltd
[61] Sandgren HR, Zhai Y, Lados DA, Shade PA, Schuren JC, Groeber MA, Kenesei P, Gavras AG (2016) Characterization of fatigue crack growth behavior in LENS fabricated Ti-6Al-4V using high-energy synchrotron x-ray microtomography. Additive Manufacturing 12:132–141, doi:10.1016/j.addma.2016.09.002, publisher: Elsevier B.V.
[62] Wainwright J, Williams S, Ding J (2023) Refinement of Ti-6Al-4V prior-β grain structure in the as-deposited condition via process control during wire-direct energy deposition. Additive Manufacturing 74:103712, doi:10.1016/j.addma.2023.103712

[63] Martin JH, Yahata B, Mayer J, Mone R, Stonkevitch E, Miller J, O'Masta MR, Schaedler T, Hundley J, Callahan P, Pollock T (2020) Grain refinement mechanisms in additively manufactured nano-functionalized aluminum. Acta Materialia 200:1022–1037, doi:10.1016/j.actamat.2020.09.043
[64] Todaro CJ, Easton MA, Qiu D, Zhang D, Bermingham MJ, Lui EW, Brandt M, StJohn DH, Qian M (2020) Grain structure control during metal 3D printing by high-intensity ultrasound. Nat Commun 11(1):142, doi:10.1038/s41467-019-13874-z
[65] Yuan D, Shao S, Guo C, Jiang F, Wang J (2021) Grain refining of Ti-6Al-4V alloy fabricated by laser and wire additive manufacturing assisted with ultrasonic vibration. Ultrasonics Sonochemistry 73:105472, doi:10.1016/j.ultsonch.2021.105472
[66] Desktop Metal (2021), Ti64 Titanium Alloy Material Datasheet
[67] Galarraga H, Lados DA, Dehoff RR, Kirka MM, Nandwana P (2016) Effects of the microstructure and porosity on properties of Ti-6Al-4V ELI alloy fabricated by electron beam melting (EBM). Additive Manufacturing 10:47–57, doi:10.1016/j.addma.2016.02.003, publisher: Elsevier B.V.
[68] Kasperovich G, Hausmann J (2015) Improvement of fatigue resistance and ductility of TiAl6V4 processed by selective laser melting. Journal of Materials Processing Technology 220:202–214, doi:10.1016/j.jmatprotec.2015.01.025, publisher: Elsevier Ltd
[69] Chen Lj, Li T, Li Ym, He H, Hu Yh (2009) Porous titanium implants fabricated by metal injection molding. Transactions of Nonferrous Metals Society of China 19(5):1174–1179, doi:10.1016/S1003-6326(08)60424-0
[70] ASM International (1990), ASM Handbook Volume 2: Properties and Selection: Nonferrous Alloys and Special-Purpose Materials
[71] Rani SU, Kesavan D, Kamaraj M (2023) Evaluation of influence of microstructural features of LPBF Ti-6Al-4 V on mechanical properties for an optimal strength and ductility. Journal of Alloys and Compounds 960:170575, doi:10.1016/j.jallcom.2023.170575
[72] Singh PK, Kumar S, Jain PK, Dixit US (2023) Effect of Build Orientation on Metallurgical and Mechanical Properties of Additively Manufactured Ti-6Al-4V Alloy. Journal of Material Engineering and Performance 33:3476–3493
[73] Froes FHS (2007) Advances in titanium metal injection molding. Powder Metall Met Ceram 46(5-6):303–310, doi:10.1007/s11106-007-0048-y
[74] Sneddon S, Xu Y, Dixon M, Rugg D, Li P, Mulvihill DM (2021) Sensitivity of material failure to surface roughness: A study on titanium alloys Ti64 and Ti407. Materials & Design 200:109438, doi:10.1016/j.matdes.2020.109438
[75] Lebea L, Ngwangwa HM, Desai D, Nemavhola F (2021) Experimental investigation into the effect of surface roughness and mechanical properties of 3D-printed titanium Ti-64 ELI after heat treatment. Int J Mech Mater Eng 16(1):16, doi:10.1186/s40712-021-00138-2
[76] Sachtleber M, Zhao Z, Raabe D (2002) Experimental investigation of plastic grain interaction. Materials Science and Engineering: A 336(1-2):81–87, doi:10.1016/S0921-5093(01)01974-8
[77] Héripré E, Dexet M, Crépin J, Gélébart L, Roos A, Bornert M, Caldemaison D (2007) Coupling between experimental measurements and polycrystal finite element calculations for micromechanical study of metallic materials. International Journal of Plasticity 23(9):1512–1539, doi:10.1016/j.ijplas.2007.01.009
[78] Zhang N, Tong W (2004) An experimental study on grain deformation and interactions in an Al-0.5%Mg multicrystal. International Journal of Plasticity 20(3):523–542,

doi:10.1016/S0749-6419(03)00100-1
[79] Tatschl A, Kolednik O (2002) On the experimental characterization of crystal plasticity in polycrystals. Materials Science and Engineering doi:10.1016/S0921-5093(03)00095-9
[80] Schroeter BM, McDowell DL (2003) Measurement of deformation fields in polycrystalline OFHC copper. International Journal of Plasticity 19(9):1355–1376, doi:10.1016/S0749-6419(02)00040-2
[81] Fang M, Li Y, Han Y, Le J, Huang G, Chai X, Lei L, Lu W (2022) In-situ investigation on the anisotropic behavior of the additively manufactured dual-phase Ti-6Al-4V alloy. Materials Characterization 189:112003, doi:10.1016/j.matchar.2022.112003
[82] ASM International (1990), ASM Handbook Volume 12: Fractography

Supplementary Information

Mechanical characterization of additive-manufactured Ti-6Al-4V processed via bound metal deposition

Eathan Devine[1], Michael Lester[1], Tanner McElroy[1],Teresa Valenzuela[1], William LePage[1,†]

[1] Department of Mechanical Engineering, University of Tulsa, Tulsa, OK, 74104, USA
[†] Correspondence: lepage@utulsa.edu

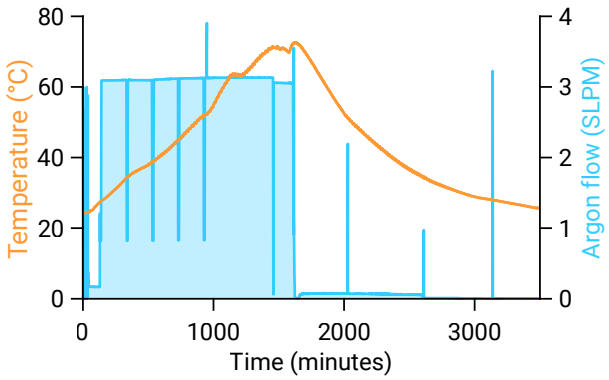

Fig. S1: *Temperature profile of two averaged RTDs placed on the outside of the furnace during a titanium sintering run, and the argon gas flow rate into the furnace during the same run. The maximum temperature was held for about 240 min, which is in the range of typical sintering times for MIM titanium.[56] The samples were then furnace cooled slowly. It is interesting to note that the UHPA flow appears to stop after the high temperature sintering hold. While the vacuum pump is likely still running at this time, the vacuum may not not reach a low enough pressure to keep contaminants under control. This may be a contributing factor leading to the high contaminant content observed in this work.*

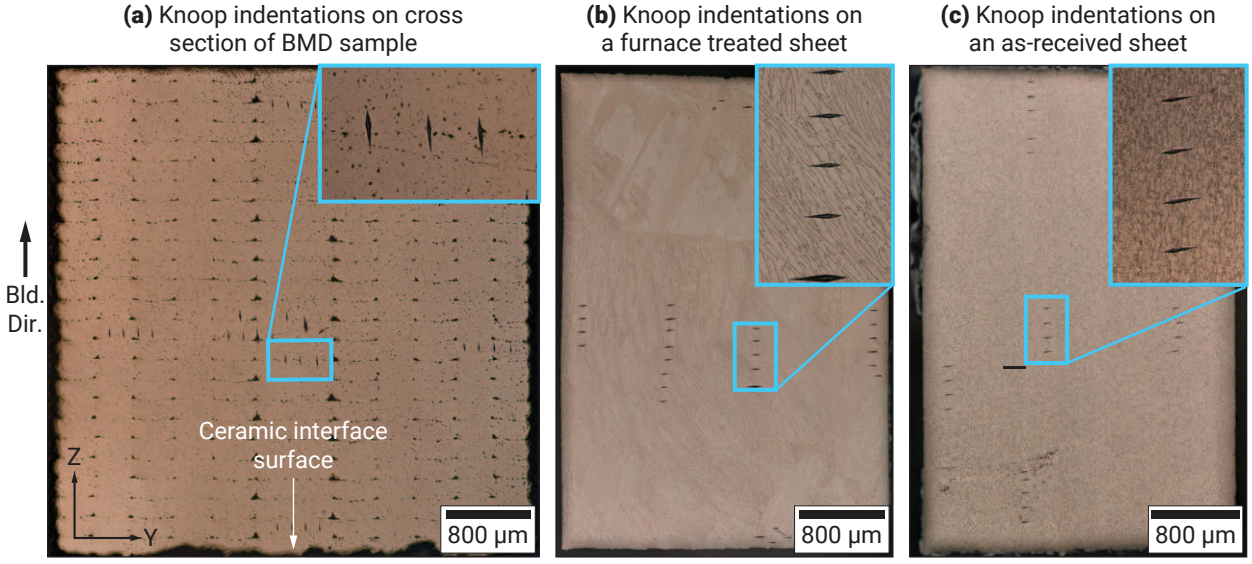

Fig. S2: *Polished cross sections of tensile specimens showing Knoop indentations of (a), an unetched BMD sample, (b), an etched FT sheet sample, and (c), an etched as-received sheet sample.*

(a) DIC setup with BMD sample in the load frame grips

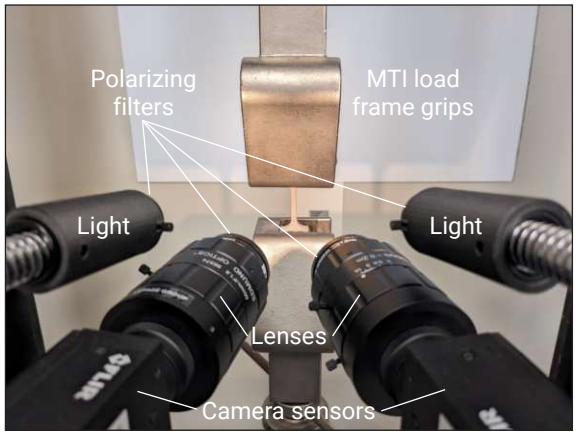

(a) BMD sample DIC speckle pattern

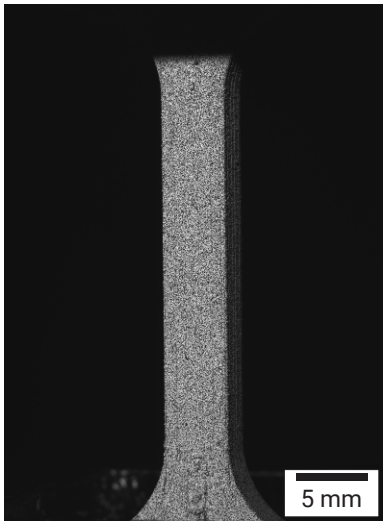

Fig. S3: *(a) A photo of the DIC setup showing the cameras with lenses, fiber optic lights, polarizing filters, load frame grips, and the BMD sample. (b) A speckled image of a BMD sample taken during DIC acquisition with an approximate pattern feature size of 50 μm.*

Table S1: *Statistical data for green sample mass and dimensions.*

Statistics	Mass	Gauge width	Thickness	Radius of fillet	Overall length	Reduced section length	Grip section length	Grip section to grip section	Grip section width	Diameter of pin hole	Edge to pin hole	Fillet to pin hole
Sample count	12	12	12	12	12	12	12	12	12	12	12	12
Maximum	70.53	5.04	5.39	8.35	98.30	26.79	27.59	43.24	27.52	8.87	11.80	9.77
Minimum	70.03	4.96	5.34	8.19	97.79	26.28	27.50	42.89	27.36	8.77	11.71	9.70
Mean	70.25	4.99	5.37	8.27	98.09	26.55	27.55	43.09	27.42	8.82	11.75	9.74
Mediam	70.23	4.98	5.38	8.27	98.19	26.56	27.54	43.13	27.41	8.83	11.76	9.75
Range	0.50	0.08	0.04	0.16	0.52	0.52	0.09	0.35	0.16	0.10	0.09	0.06
Std. Dev.	0.14	0.02	0.01	0.05	0.18	0.16	0.03	0.13	0.04	0.03	0.03	0.02

Table S2: *Statistical data for brown sample mass and dimensions.*

Statistics	Mass	Gauge width	Thickness	Radius of fillet	Overall length	Reduced section length	Grip section length	Grip section to grip section	Grip section width	Diameter of pin hole	Edge to pin hole	Fillet to pin hole
Sample count	12	12	12	12	12	12	12	12	12	12	12	12
Maximum	66.51	4.99	5.55	8.47	98.02	26.59	27.47	43.08	27.39	8.74	11.74	9.80
Minimum	66.02	4.94	5.45	8.22	97.70	26.01	27.29	42.88	27.21	8.59	11.68	9.75
Mean	66.25	4.96	5.48	8.40	97.82	26.16	27.37	42.97	27.30	8.65	11.71	9.77
Mediam	66.25	4.97	5.47	8.44	97.82	26.10	27.38	42.95	27.31	8.63	11.72	9.76
Range	0.49	0.06	0.10	0.24	0.32	0.58	0.18	0.20	0.18	0.15	0.06	0.06
Std. Dev.	0.14	0.02	0.04	0.07	0.10	0.16	0.05	0.05	0.05	0.05	0.02	0.02

Table S3: *Statistical data for sintered sample mass and dimensions.*

Statistics	Mass	Gauge width	Thickness	Radius of fillet	Overall length	Reduced section length	Grip section length	Grip section to grip section	Grip section width	Diameter of pin hole	Edge to pin hole	Fillet to pin hole
Sample count	12	12	12	12	12	12	12	12	12	12	12	12
Maximum	63.73	4.38	4.47	6.85	85.99	24.26	24.25	37.87	24.21	7.68	10.27	8.53
Minimum	63.27	4.32	4.36	6.79	85.65	23.83	23.99	37.48	23.99	7.59	10.22	8.48
Mean	63.47	4.36	4.41	6.82	85.80	24.02	24.11	37.66	24.10	7.61	10.24	8.50
Mediam	63.45	4.36	4.40	6.83	85.79	24.01	24.11	37.62	24.12	7.61	10.24	8.50
Range	0.46	0.06	0.11	0.06	0.34	0.42	0.27	0.38	0.22	0.09	0.04	0.05
Std. Dev.	0.13	0.02	0.03	0.02	0.11	0.11	0.07	0.11	0.07	0.03	0.01	0.01

Table S4: *Overall and interlayer porosity, both calculated with the same pixel threshold value of 0.65, meaning that the MATLAB script maps pixel values between 0 and 0.65 to values between 0.5 and 1 in order to best determine which pixels represent pores.*

Specimen ID	Overall porosity (%)	Interlayer porosity (%)
04412	2.406	1.369
12431	0.969	0.338
14243	1.194	0.288

Table S5: *Microhardness statistics for BMD samples in **Fig. S2**.*

Statistics	Left	Right	Top	Bottom	Middle
Sample count	2	2	2	2	2
Indentation count	9	7	9	4	8
Maximum	430.37	437.77	440.82	478.76	392.16
Minimum	275.98	319.77	260.62	346.03	205.14
Mean	359.31	381.15	355.28	408.79	296.38
Mediam	369.61	388.58	356.86	405.19	299.54
Range	154.39	117.99	180.21	132.72	187.03
Std. Dev.	53.4371	38.9449	48.8823	49.0377	50.5113

Table S6: *Microhardness statistics for FT sheet samples in **Fig. S2**.*

Statistics	Left	Right	Top	Bottom	Middle
Sample count	2	2	2	2	2
Indentation count	7	8	7	7	16
Maximum	454.37	438.11	460.45	525.33	541.63
Minimum	179.31	241.43	351.26	199.36	188.42
Mean	329.13	380.44	391.44	368.00	338.22
Mediam	360.59	402.55	384.16	360.59	338.75
Range	275.06	196.68	109.19	325.97	353.21
Std. Dev.	82.8326	59.6772	34.8895	113.181	76.3862

Table S7: *Software details for DIC.*[47]

DIC Software	Vic-3D 9
Image Filtering	Low-pass filtering
Subset Size	27 – 31
Step Size	5 – 7
Subset Shape Function	Gaussian Weights
Strain Formulation	Lagrange
Strain Window	11
Calibration Target	Correlated Solutions glass 4-in-1
Focal Length	Camera 1: 16919.9 pixel; Camera 2: 16829.2 pixel
Stereo-Angle	32.2217
Distance between Cameras	100.117 mm
Reference Image	Single reference image (standard correlation)
Interpolant	Optimized 8-tap
Matching Criterion	Zero-normalized squared differences

Table S8: *Hardware details for DIC.*[47]

Camera	FLIR GS3-U3-123S6M-C
Image Resolution	4096 x 3000
Lens	Edmund Optics HP Series 50 mm (#86-574)
FOV	43.65 mm x 31.97 mm
Image Scale	93.827 pixel/mm
Stereo-Angle	32.2217
SOD	$\sim$200 mm
Image Acquisition Rate	0.5 Hz
Patterning Technique	Black speckles on white base coat
Approximate Pattern Feature Size	$\sim$50 µm
Aperture	f/14